



Call: H2020-SC5-2014-two-stage

Topic: SC5-01-2014

**PRIMAVERA**

Grant Agreement 641727



**PRocess-based climate sIMulation: AdVances in high resolution modelling and European climate Risk Assessment**

## **Deliverable D3.4**

**Quantification of the benefits of enhanced upper ocean mixing processes on the European climate system and robustness across the multi-model resolution ensemble**

Deliverable Title	<i>Quantification of the benefits of enhanced upper ocean mixing processes on the European climate system and robustness across the multi-model resolution ensemble</i>	
Brief Description	<i>This deliverable assesses the impact of new upper ocean mixing schemes on the performance of ocean models used in PRIMAVERA, specifically the IDEMIX scheme for internal wave mixing in the MPI ocean model, and the OSMOSIS scheme for Langmuir turbulence in the NEMO ocean model.</i>	
WP number	3	
Lead Beneficiary	<i>Adrian New, National Oceanography Centre</i>	
Contributors	<i>Oliver Gutjahr, Johann Jungclaus, Max-Planck Institute George Nurser, National Oceanography Centre Catherine Guiavarch, Met Office Dan Copsey, Met Office</i>	
Creation Date	13 February 2020	
Version Number	2	
Version Date	27 February 2020	
Deliverable Due Date	30 November 2019	
Actual Delivery Date	27 February 2020	
Nature of the Deliverable	<input checked="" type="checkbox"/>	<i>R - Report</i>
	<input type="checkbox"/>	<i>P - Prototype</i>
	<input type="checkbox"/>	<i>D - Demonstrator</i>
	<input type="checkbox"/>	<i>O - Other</i>
Dissemination Level/ Audience	<input type="checkbox"/>	<i>PU - Public</i>
	<input checked="" type="checkbox"/>	<i>PP - Restricted to other programme participants, including the Commission services</i>
	<input type="checkbox"/>	<i>RE - Restricted to a group specified by the consortium, including the Commission services</i>
	<input type="checkbox"/>	<i>CO - Confidential, only for members of the consortium, including the Commission services</i>

Version	Date	Modified by	Comments
1	13/2/2019	Adrian New	Initial version
2	27/2/2019	Adrian New	Final version

## **Table of Contents**

1. Executive Summary .....	5
2. Project Objectives .....	6
3. Detailed Report .....	7
3.1 The IDEMIX scheme (MPI – Oliver Gutjahr, Johann Jungclaus).....	8
3.1.1 The vertical mixing schemes based on TKE and IDEMIX in MPI-ESM1.2.....	8
3.1.2 Experiments.....	9
3.1.3 Results.....	10
3.1.4 Key Points and Conclusions.....	21
3.2 The OSMOSIS OSBL scheme (NOC/Met Office).....	23
3.2.1 Description of the OSMOSIS OSBL scheme.....	23
3.2.2 Model Implementation .....	27
3.2.3 Results.....	27
3.2.4 Key Points and Conclusions.....	37
4. Lessons Learnt.....	38
5. Links Built .....	38
References.....	39

**List of Figures**

Figure 1: Time-averaged vertical diffusivity coefficient  $\log_{10}(K)$  ( $m^2 s^{-1}$ ) at a depth of 1020 m in the MPI-ESM1.2-HR simulations for (a) HR<sub>pp</sub>, (b) HR<sub>kpp</sub>, (c) HR<sub>tke</sub>, and (d) HR<sub>ide</sub>. ..... 10

Figure 2: Potential temperature bias at 740 m depth of MPI-ESM1.2-HR minus EN4 (1945-1955) for (a) HR<sub>pp</sub>, (b) HR<sub>kpp</sub>, (c) HR<sub>tke</sub>, and (d) HR<sub>ide</sub>. ..... 11

Figure 3: Salinity bias at 740 m depth of MPI-ESM1.2-HR minus EN4 (1945-1955) for (a) HR<sub>pp</sub>, (b) HR<sub>kpp</sub>, (c) HR<sub>tke</sub>, and (d) HR<sub>ide</sub>. ..... 12

Figure 4: Zonal-mean bias of potential temperature to EN4 (1945-1955) in the Atlantic and Arctic Ocean for (a) HR<sub>pp</sub>, (b) HR<sub>kpp</sub>, (c) HR<sub>tke</sub>, and (d) HR<sub>ide</sub>. ..... 13

Figure 5: Circulation in the Nordic seas and at Fram Strait at a depth of 220m simulated by MPI-ESM1.2 (a) HR<sub>pp</sub>, (b) HR<sub>kpp</sub>, (c) HR<sub>tke</sub>, and (d) HR<sub>ide</sub>. Indicated by the arrow length at the bottom right is the reference velocity. .... 15

Figure 6: Temperature bias at 420m depth to EN4 for (a) HR<sub>pp</sub>, (b) HR<sub>kpp</sub>, (c) HR<sub>tke</sub>, and (d) HR<sub>ide</sub>. ..16

Figure 7: Time-averaged vertical diffusivity coefficient  $\log_{10}(K)$  ( $m^2 s^{-1}$ ) in the Arctic Ocean at a depth of 690 m in the MPI-ESM1.2-HR simulations for (a) HR<sub>pp</sub>, (b) HR<sub>kpp</sub>, (c) HR<sub>tke</sub>, and (d) HR<sub>ide</sub>. ..... 17

Figure 8: Time-averaged vertical diffusivity coefficient  $\log_{10}(K)$  ( $m^2 s^{-1}$ ) at a depth of 690 m in the MPI-ESM1.2-HR simulations for (a) HR<sub>pp</sub>, (b) HR<sub>kpp</sub>, (c) HR<sub>tke</sub>, and (d) HR<sub>ide</sub>. ..... 18

Figure 9: Time-averaged mixed layer depths (m) in March calculated (a) from  $1^\circ \times 1^\circ$  Argo float data (Holte et al., 2017) from January 2000 to April 2018 by the density threshold method ( $\sigma_t = 0.03 \text{ kg m}^{-3}$ ) and with  $\sigma_t = 0.01 \text{ kg m}^{-3}$  from MPI-ESM1.2 (b) HR<sub>pp</sub>, (c) HR<sub>kpp</sub>, (d) HR<sub>tke</sub>, and (e) HR<sub>ide</sub>. ..... 19

Figure 10: Time-averaged barotropic volume transport function for (a) HR<sub>pp</sub>, and the differences (b) HR<sub>kpp</sub> - HR<sub>pp</sub>, (c) HR<sub>tke</sub> - HR<sub>pp</sub>, and (d) HR<sub>ide</sub> - HR<sub>pp</sub>. ..... 20

Figure 11: Eulerian stream function ( $Sv \ 10^6 \text{ m}^3 \text{ s}^{-1}$ ) of the AMOC in depth space for (a) HR<sub>pp</sub>, (b) HR<sub>kpp</sub>, (c) HR<sub>tke</sub>, and (d) HR<sub>ide</sub>. ..... 22

Figure 12: The structure of the entraining boundary layer. Profiles of (a) mean buoyancy (b) buoyancy flux. .... 24

Figure 13: MLD in February from (a) ARGO climatology (Holte et al., 2017) and (b) as simulated at  $1^\circ$  resolution using the standard NEMO TKE model. .... 28

Figure 14: Variation with latitude of zonal-mean MLD in the SH (Southern Hemisphere) in February. (a) For the Holte climatology (blue line) and for the standard TKE model (orange line) and adjusted TKE model (green line); (b) For the standard OSMOSIS model (green line) the standard TKE model (red line) and the sub-mesoscale-aware OSMOSIS model (orange line: OSMOSIS coupled to the Fox-Kemper scheme, see below). .... 29

Figure 15: February MLD as simulated by NEMO with the OSMOSIS model. (a) MLD and (b) deviation from Holte climatology. .... 29

Figure 16: Deviations from Reynolds climatological February SST. (a) for standard (nn\_etau=0) TKE model and (b) OSMOSIS .....30

Figure 17: (a) February Zonal mean SSTs and (b) deviations from the Reynolds climatology for OSMOSIS, the standard TKE (nn\_etau=0, TKE0) and adjusted TKE (nn\_etau=1, TKE1).....30

Figure 18: Zonally averaged MLDs in the Southern Hemisphere (SH) in August. Climatology (blue), OSMOSIS (green), standard TKE (red) and OSMOSIS-FK (orange).....31

Figure 19: Met. O. CORE-II forced 1/4 ° ocean-only runs. Austral summer (DJF) MLD averages. Run u-bj912 is the OSMOSIS run and u-bj503 the comparison run with TKE (and nn\_etau=1). The bottom two figures show the differences with the De Boyer-Montegut climatology.....32

Figure 20. As Fig. 19 but for northern summer (average JJA) MLDs.....33

Figure 21. As for Fig. 19 but for Southern summer SST (average DJF), and now compared with the ESA CCI satellite SSTs.....34

Figure 22. As Fig. 21 but for northern summer SST (average JJA).....34

Figure 23. Southern summer (DJF) averages of MLD. Run u-bo640 is the coupled OSMOSIS run and u-bo921 the comparison run with TKE (and nn\_etau=1) .....35

Figure 24. Northern summer (JJA averages) of MLD. Run u-bo640 is the OSMOSIS run and u-bo921 the comparison run with TKE (and nn\_etau=1).....36

Figure 25. Southern summer (DJF) averages of SST for the coupled runs.....36

Figure 26. Northern summer (JJA) averages of SST for the coupled runs .....37

## **1. Executive Summary**

This report summarises the impact of including advanced schemes which represent upper ocean mixing processes in ocean general circulation models. Rather than the usual basic parameterisations of such mixing, we here discuss two schemes which include key processes in a realistic manner. These are, firstly, mixing from internal wave breaking below the upper well-mixed layer (in the IDEMIX scheme) and that arising from Langmuir turbulence (resulting from the interaction of the wind and waves) in the mixed layer itself (OSMOSIS).

Although the effects of IDEMIX are generally of second order importance as compared to the increase in resolution from 0.4° to 0.1° in the MPI model, the scheme, through the realistic simulation of internal wave mixing effects, is able to reduce the amount of spurious warm Atlantic Water flowing into the Arctic to the same level as provided by such an increase in resolution. The more realistic representation of this effect is not only important for the Arctic Ocean but might also impact European climate, as the heat content of the Arctic Ocean

influences the atmospheric meridional temperature gradient and thus the westward wind strength of the Jet Stream.

The OSMOSIS scheme has been tested in 1° and ¼° forced ocean (NEMO) models and in a coupled N96 atmosphere - ¼° ocean model. Generally, this is found to reduce the warm bias in the Southern Ocean (a major bias typical in ocean and climate models), although it also gives Mixed Layer Depths (MLDs) which are too deep here in winter. However, current work is linking the OSMOSIS scheme to the Fox-Kemper scheme which allows an upward vertical buoyancy flux through the mixed layer base from sub-mesoscale motions. The inclusion of this realistic process is effective in reducing these deep winter MLDs, though further work is still needed to optimize the coupling between the two processes. For the North Atlantic, the winter Sea-Surface Temperature (SST) bias in the 1° model is reduced when using the OSMOSIS scheme as compared with the standard existing mixing scheme in NEMO (TKE), which could have consequences for Europe in terms of better air-sea fluxes and Jet Stream properties. A larger reduction to this cold bias may also be achieved by utilising a ¼° resolution ocean, though at increased computer cost.

Finally, the development of IDEMIX and OSMOSIS will leave a lasting legacy for future ocean and climate modelling studies, which will thereby include more realistic representations of upper ocean mixing processes.

## 2. Project Objectives

With this deliverable, the project has contributed to the achievement of the following objectives (DOA, Part B Section 1.1) WP numbers are in brackets:

No.	Objective	Yes	No
A	To develop a new generation of global high-resolution climate models. (3, 4, 6)	x	
B	To develop new strategies and tools for evaluating global high-resolution climate models at a process level, and for quantifying the uncertainties in the predictions of regional climate. (1, 2, 5, 9, 10)		x
C	To provide new high-resolution protocols and flagship simulations for the World Climate Research Programme (WCRP)'s Coupled Model Intercomparison Project (CMIP6) project, to inform the Intergovernmental Panel on Climate Change (IPCC) assessments and in support of emerging Climate Services. (4, 6, 9)		x
D	To explore the scientific and technological frontiers of capability in global climate modelling to provide guidance for the development of future generations of prediction systems, global climate and Earth System models (informing post-CMIP6 and beyond). (3, 4)	x	
E	To advance understanding of past and future, natural and anthropogenic, drivers of variability and changes in European climate, including high impact events, by exploiting new capabilities in high-resolution global climate modelling. (1, 2, 5)		x

F	To produce new, more robust and trustworthy projections of European climate for the next few decades based on improved global models and advances in process understanding. (2, 3, 5, 6, 10)	x	
G	To engage with targeted end-user groups in key European economic sectors to strengthen their competitiveness, growth, resilience and ability by exploiting new scientific progress. (10, 11)		x
H	To establish cooperation between science and policy actions at European and international level, to support the development of effective climate change policies, optimize public decision making and increase capability to manage climate risks. (5, 8, 10)		x

### **3. Detailed Report**

Overall, good progress was made towards including IDEMIX and OSMOSIS into the respective ocean models but this was slower than originally anticipated (due to the complex nature of the schemes and their interactions with the other processes included in the models). This meant that IDEMIX was only able to undertake a reduced set of PRIMAVERA (Stream 2) coupled ocean-atmosphere simulations and OSMOSIS was able to undertake only ocean-only simulations together with a trial coupled simulation. We were also unable to fully investigate their impact on European climate, though their effects seem likely to be smaller than increasing the ocean model resolution to eddy-permitting or eddy-resolving levels. Furthermore, due to change of personnel, KNMI did not contribute to the development of these schemes, undertaking alternate work instead. Nonetheless, there was no impact on other tasks, and significant simulations in coupled models have been undertaken with both schemes, leading to interesting scientific results as described below. This is expected to lead to the publication of scientific papers in due course. The schemes will also leave a lasting legacy for future ocean and climate modelling studies. The report was delayed from its original submission date to allow for the inclusion of the description of coupled runs with the OSMOSIS scheme, to the benefit of the overall deliverable.

In more detail, and with reference to the Description of Work (DOW), task T3D.1 was undertaken by NERC (now NOC), with the assistance of the Met Office, and additional work was undertaken towards coupling the OSMOSIS scheme to the Fox-Kemper scheme for re-stratification by sub-mesoscale eddies. Task T3D.2 was undertaken by MPG (now MPI) with work on the mixing generated by internal waves at the base of the mixed layer.

### 3.1 The IDEMIX scheme (MPI – Oliver Gutjahr, Johann JungCLAUS)

Vertical or diapycnal mixing is one of the most important processes that cannot be explicitly resolved by ocean models. The energy for the background mixing must be consistently supplied by mechanical sources, such as the scattering of internal waves on topography or the energy flux in the sub-inertial band excited by winds. Whereas existing parameterisations lack this consistency and often assume constant background mixing, the approach of the newly developed Internal Wave Dissipation, Energy and Mixing (IDEMIX) scheme (Olbers and Eden, 2013; Eden et al., 2014) accounts for the wave energy budget by calculating the generation, propagation, and dissipation of the internal gravity wave field. In order to investigate the effects and potential benefits of improved ocean vertical mixing in the coupled Max Planck Institute Earth System Model (MPI-ESM1.2), we performed sensitivity experiments, in which we made use of IDEMIX. Besides the general effects of exchanging the ocean vertical mixing scheme with the pre-existing TKE scheme, we are particularly interested in the effect of the IDEMIX scheme.

#### 3.1.1 The vertical mixing schemes based on TKE and IDEMIX in MPI-ESM1.2

IDEMIX parameterizes the internal wave energy ( $E_{iw}$ ) in terms of a budget equation:

$$\frac{\partial E_{iw}}{\partial t} = \nabla_h v_0 \tau_h \nabla_h v_0 E_{iw} + \frac{\partial}{\partial z} \left( c_0 \tau_v \frac{\partial c_0 E_{iw}}{\partial z} \right) - \varepsilon_{iw}, \quad (1)$$

with  $v_0$  the lateral group velocity,  $\tau_h$  a lateral time scale on which lateral anisotropies are eliminated by nonlinear wave-wave interactions,  $c_0$  the weighted average group velocity,  $z$  the vertical coordinate,  $\tau_v$  a time scale on order of days, and  $\varepsilon_{iwe}$  the dissipation of internal wave energy. The first term on the right-hand side describes the horizontal diffusion of internal wave energy, and the second term its vertical diffusion. Internal wave energy is eventually destroyed by its dissipation.

IDEMIX models that part of the ocean between the base of the near-surface mixed layer and the ocean bottom, and is closed by prescribing the upper and lower boundary conditions. Currently, we prescribe time constant fields for the energy fluxes at the upper surface and at the bottom, as in Olbers and Eden (2013). At the upper surface, internal waves near the inertial frequency are excited at the base of the mixed layer due to temporally fluctuating wind stress, the so-called inertial pumping. The energy flux is estimated as 20% of the wind input into the inertial band of the mixed layer (Jochum et al., 2013). We neglect, however, other sources exciting internal waves near the surface, for instance buoyancy plumes that overshoot the mixed layer base, vertical roll vortices of turbulent eddies, or Langmuir circulation that undulates internal waves (Czeschel and Eden, 2019). At the bottom, barotropic tides interact with the bottom roughness and convert energy to internal waves. This energy flux is prescribed from Jayne (2009).

The dissipation of internal wave energy is parameterized following McComas and Müller (1981) as  $\varepsilon_{iwe} = \mu f E_{iw}^2 / c_*^2$ , where the parameter  $\mu = O(1)$ ,  $f$  is the Coriolis parameter, and  $c_*$  is related to the bandwidth of the Garrett-Munk (GM) spectrum in wavenumber space. The process that leads to dissipation is the breaking of internal waves. This breaking of internal waves transfers energy to small-scale turbulent kinetic energy (TKE), the dissipation of which eventually causes mixing. In commonly used vertical mixing schemes, such as KPP (Large et al., 1994) or TKE (Gaspar et al., 1990), this breaking of internal waves is usually parameterized by simply assuming a constant background diffusivity (either a scalar or vertical profile). By using IDEMIX, the constant background diffusivity is replaced by a prognostic equation for internal wave energy and thus for its dissipation, as described above. We use the recommended parameter set from Pollmann et al., (2017).

The modified TKE equation (Eden et al., 2014) then reads:

$$\frac{d\bar{E}_{tke}}{dt} = -\partial_z(\text{fluxes}) + c_u K (\partial_z \bar{\mathbf{u}})^2 - c_b K N^2 - \varepsilon_{tke} + \varepsilon_{iw}, \quad (2)$$

with the dimensionless parameters  $c_u$  and  $c_b$ , which are related by  $c_u = c_b R_i / R_f$ . The first term on the right-hand side describes the redistribution of TKE in the vertical. Surface fluxes enter as boundary conditions to this term. The second term describes the vertical momentum fluxes acting on the shear of the mean flow, transferring energy from the mean flow to TKE. The third term is the buoyancy term that transfers energy to the potential energy of the mean flow, thereby decreasing TKE. The dissipation of TKE (fourth term) is parameterized as  $\varepsilon_{tke} = \bar{E}_{tke}^{2/3} L^{-1}$  with the mixing length  $L = \sqrt{2\bar{E}_{tke} / N^2}$  (Blanke and Delecluse, 1993; Eden et al., 2014). The last term on the right-hand side is then the (optional) contribution from the internal wave breaking from IDEMIX.

The diffusivity is parameterized as  $K = \bar{E}_{tke}^{1/2} L$  by assuming the same mixing length as for the dissipation. If the internal wave breaking term is not considered, then a background diffusivity is assumed to represent internal wave breaking (Eden et al., 2014). When a minimum value for TKE is used, we set  $E_{\min} = 10^{-6} \text{ m}^2 \text{ s}^2$  and the background diffusivity is then defined as  $K = \sqrt{2} E_{\min} / N$ .

### 3.1.2 Experiments

We performed four 100-year control simulations with the MPI-ESM1.2-HR (high resolution model, using a resolution of  $0.4^\circ$  in the ocean and about  $1^\circ$  (T127) in the atmosphere) using four different ocean vertical mixing schemes. The reference simulation uses the Pacanowski and Philander (1981) or PP scheme ( $\text{HR}_{pp}$ ), which was also used to tune MPI-ESM1.2. In the second simulation we used the K-profile parameterisation (KPP; Large et al., 1994) and refer to it as  $\text{HR}_{kpp}$ . This simulation is also part of HighResMIP (Gutjahr et al., 2019).

Based on the TKE scheme described above, we used the TKE scheme for the third simulation with a prescribed background diffusivity ( $E_{\min} = 10^{-6} \text{ m}^2\text{s}^2$ ) and set  $\varepsilon_{iw} = 0$ . We refer to this experiment as  $\text{HR}_{\text{tke}}$ . In the last experiment, we did not use a constant background diffusivity, but set  $E_{\min} = 0 \text{ m}^2\text{s}^2$  and used the prognostic equation for  $\varepsilon_{iw}$  from IDEMIX. We refer to this experiment as  $\text{HR}_{\text{ide}}$ .

The initial state for all simulations was an MPI-ESM1.2-HR simulation (with the PP scheme) that was nudged to the average state of 1950 to 1954 of the Met Office Hadley Centre EN4 observational data set (version 4.2.0; Good et al., 2013). All simulations were forced by constant 1950s forcing, following the HighResMIP protocol (Haarsma et al., 2016) over an integration time of 150 years (only 100 years for  $\text{HR}_{\text{kpp}}$ ). As recommended in the protocol, the model was not re-tuned in order to obtain unbiased effects from the change of the ocean vertical mixing scheme.

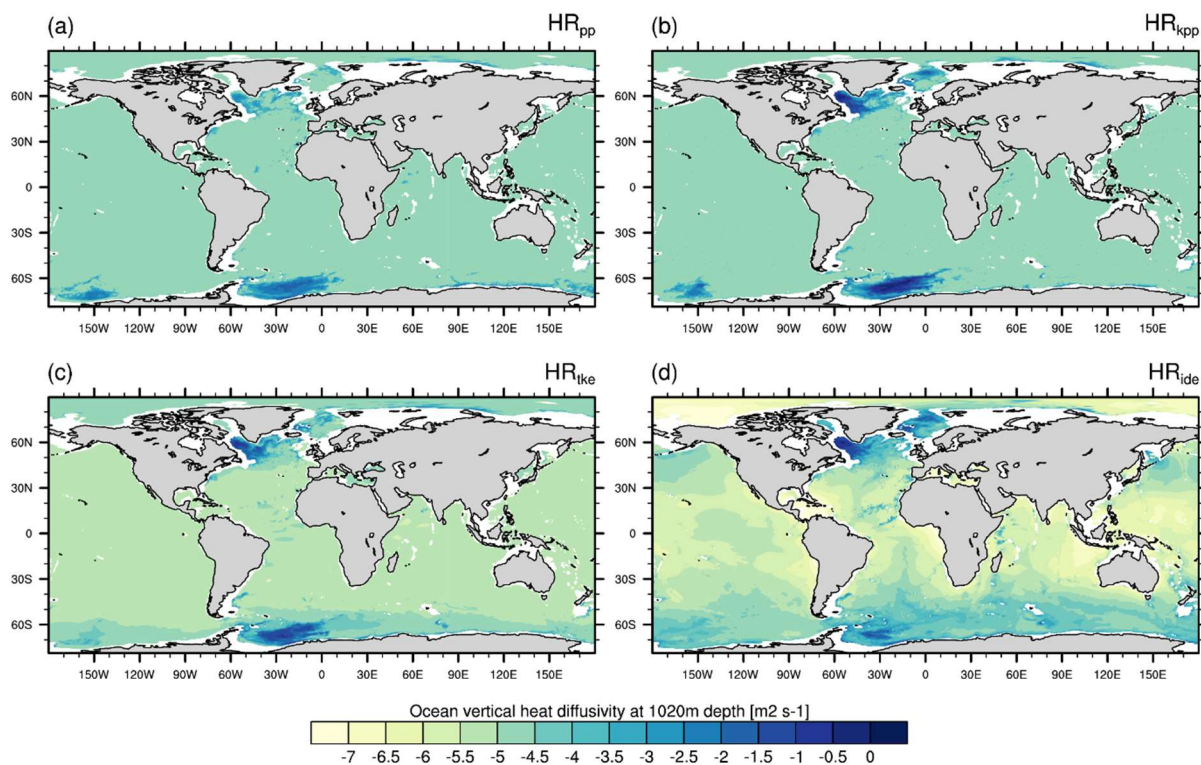


Figure 1: Time-averaged vertical diffusivity coefficient  $\log_{10}(K)$  ( $\text{m}^2 \text{s}^{-1}$ ) at a depth of 1020 m in the MPI-ESM1.2-HR simulations for (a)  $\text{HR}_{\text{pp}}$ , (b)  $\text{HR}_{\text{kpp}}$ , (c)  $\text{HR}_{\text{tke}}$ , and (d)  $\text{HR}_{\text{ide}}$ .

### 3.1.3 Results

In the following, we investigate how this improved vertical mixing scheme affects the mean state of the ocean and atmosphere in control simulations with MPI-ESM1.2-HR. For all comparisons, we averaged the model years 80 to 100.

### 3.1.3.1 Spatial distribution of $K$

Fig. 1 shows a global map of the vertical diffusivity  $K$  at a depth of 1020 m. The spatial distribution of  $K$  is homogeneous for large parts of the global ocean to leading order; in the cases of  $HR_{pp}$  and  $HR_{kpp}$  it is at the background value of  $K = 1.05 \cdot 10^{-4} \text{ m}^2\text{s}^{-2}$ .  $HR_{tke}$  simulates a background mixing of about one order less in most of the subtropical and tropical ocean. The distribution of  $K$  is much more heterogeneous in  $HR_{ide}$ , with higher mixing above rough topography and mixing coefficients of about two orders of magnitude lower above abyssal plains and in the Arctic Ocean. Hot spots of strong vertical mixing are simulated in the subpolar North Atlantic (SPNA), in the Nordic seas, and in the Weddell and Ross Sea of the Southern Ocean. Excessive deep convection in the Weddell Sea is a known issue in ocean models and not unique to MPI-ESM1.2-HR. The unrealistic convection (and strong vertical mixing) is related to too frequent open-ocean Weddell Sea polynyas in the model. Although  $HR_{ide}$  reduces deep convection in this area, we do not discuss it further here.

A closer look at Fig.1 reveals further differences in the above-mentioned areas, which we will discuss in the following. We will further relate these differences to the temperature and salinity bias in the Atlantic, GIN/Nordic seas, and Arctic Ocean.

### 3.1.3.2 Temperature and salinity bias

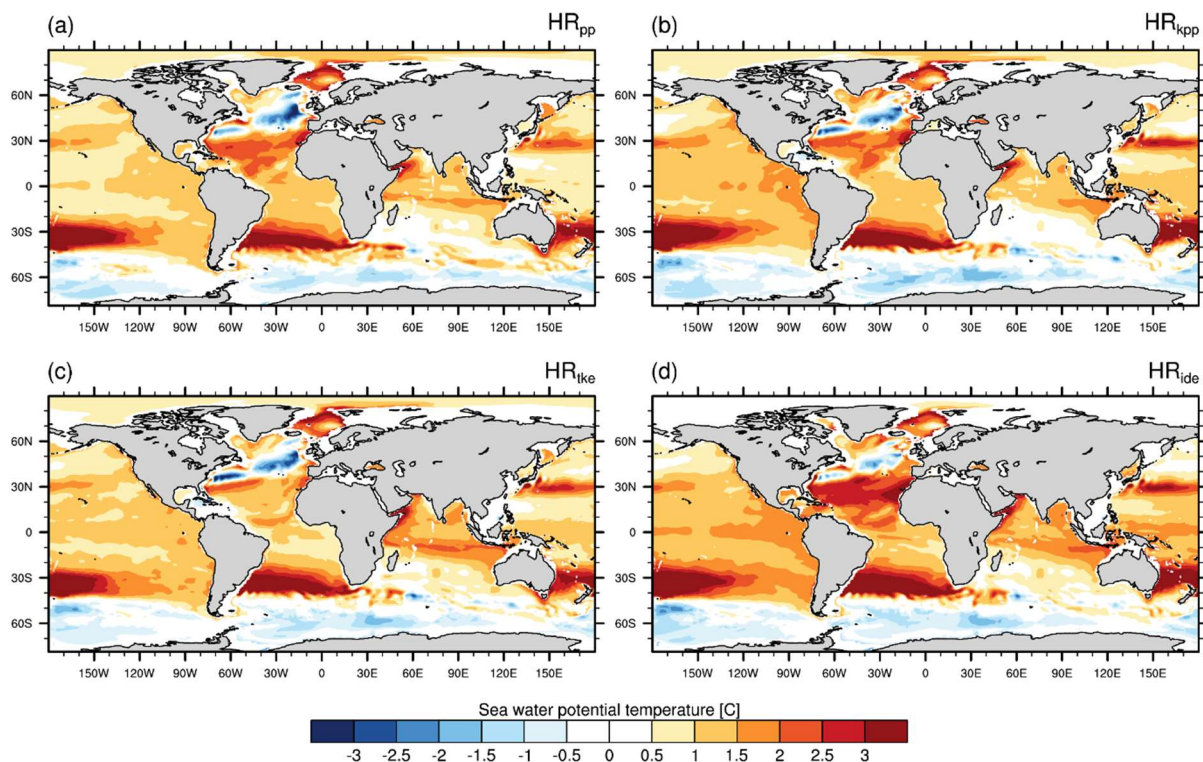


Figure 2: Potential temperature bias at 740 m depth of MPI-ESM1.2-HR minus EN4 (1945-1955) for (a)  $HR_{pp}$ , (b)  $HR_{kpp}$ , (c)  $HR_{tke}$ , and (d)  $HR_{ide}$ .

All simulations show mostly a too warm upper ocean, as exemplified for the temperature at

740 m depth (Fig. 2). An exception where the upper ocean is too cold with respect to EN4 is the Southern Ocean and parts of the North Atlantic. In the Atlantic Ocean, the warm biases are mainly linked to wrong representations of the Agulhas Current System, Mediterranean Overflow water (MOW) and the pathway of the Gulf Stream (Gutjahr et al., 2019, Putrasahan et al., 2019). Subsequent warm biases, e.g. in the Subpolar North Atlantic (SPNA), Nordic seas and Arctic Ocean, are a direct consequence of advecting these too warm (and saline) water masses. To a first order, all simulations show similar biases. As concluded by Gutjahr et al., (2019), these biases are mainly associated with the rather coarse model resolution in HR ( $0.4^\circ$ ). These biases are mitigated when a higher resolution in the ocean is used, e.g.  $0.1^\circ$  as was demonstrated by Gutjahr et al., (2019) for MPI-ESM1.2-ER.

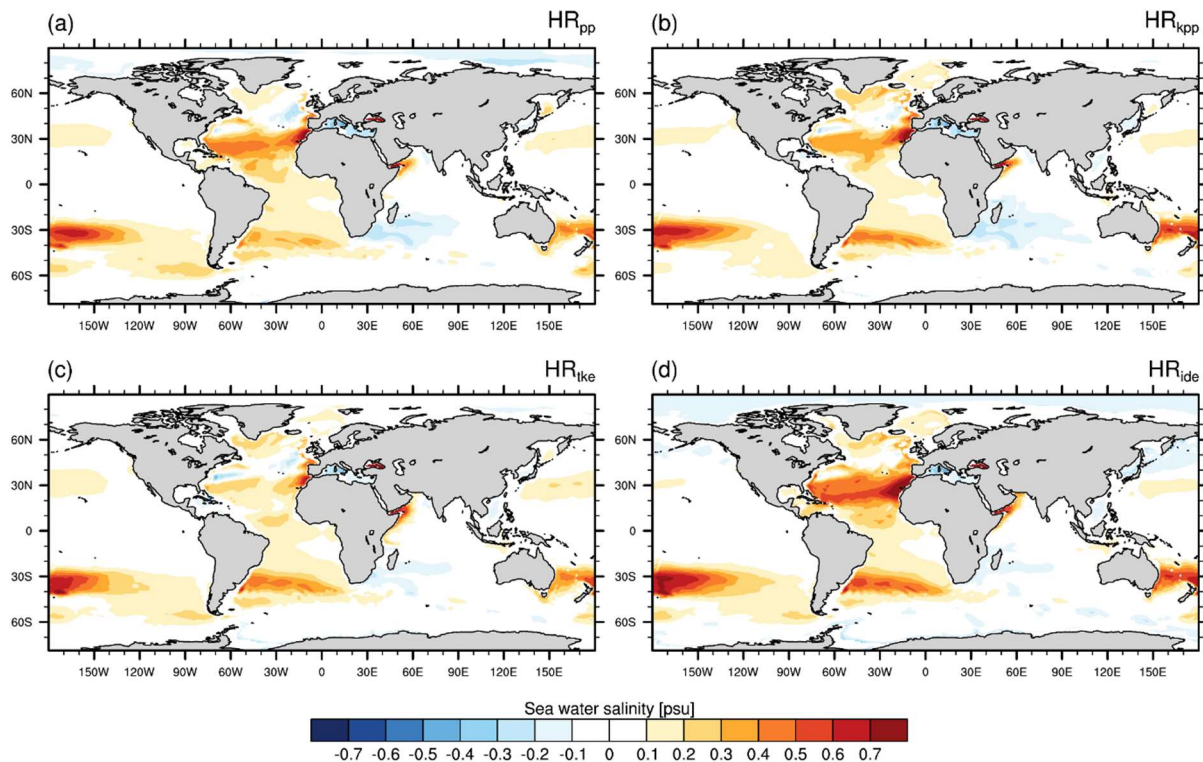


Figure 3: Salinity bias at 740 m depth of MPI-ESM1.2-HR minus EN4 (1945-1955) for (a) HR<sub>pp</sub>, (b) HR<sub>kpp</sub>, (c) HR<sub>tke</sub>, and (d) HR<sub>ide</sub>.

As with the temperature, the salinity in the upper ocean (Fig.3) shows a similar bias pattern, with mainly too high salinity in the Atlantic. Most prominent are positive salinity biases related to the MOW and the Agulhas. The too saline waters are then advected into the subpolar North Atlantic, either by the Gulf Stream or by the boundary current along the European Shelf. Although all simulations show similar salinity biases, we notice some differences. First, HR<sub>kpp</sub>, HR<sub>tke</sub>, and HR<sub>ide</sub> simulate a larger bias in the South Atlantic related to the Agulhas Current. Second, these simulations show a slightly larger salinity bias in the SPNA (Sub-Polar North Atlantic), and third, the largest difference occurs for the MOW. Here, HR<sub>tke</sub> reduces the bias in comparison to HR<sub>pp</sub> and HR<sub>kpp</sub>, whereas the bias is larger in HR<sub>ide</sub>. We suspect that this larger bias results from reduced mixing in the Mediterranean Sea and, in particular, near the overflow sill and downstream of it. The latter reduces the mixing with ambient less saline waters so that

the warm, high saline core of the MOW is less diluted than in the other simulations.

A vertical section of the zonally averaged potential temperature bias through the Atlantic and Arctic Ocean (Fig. 4), shows again warm biases related to the above-named currents and water masses. Salinity shows a similar bias pattern (not shown) with too saline waters where there is a warm bias. Pronounced warm biases are simulated in the Atlantic Water Layer (AWL) in the Arctic Ocean, in the Nordic seas, for the overflow waters at roughly 60°N, for the Mediterranean Overflow Water (MOW) at 30°N at about 800 to 1000 m depth, and at roughly 40°S in relation to the Agulhas Current System. A comparison of  $HR_{kpp}$  with the reference simulation  $HR_{pp}$  reveals almost no differences, except for slightly warmer overflow waters and a slightly warmer Arctic Ocean. A similar result is found for  $HR_{tke}$ , except that the bias related to the MOW is reduced. In contrast, in  $HR_{ide}$  the warm bias in the AWL reduces in the Arctic Ocean, whereas the warm bias related to the MOW and the Agulhas Current become stronger.

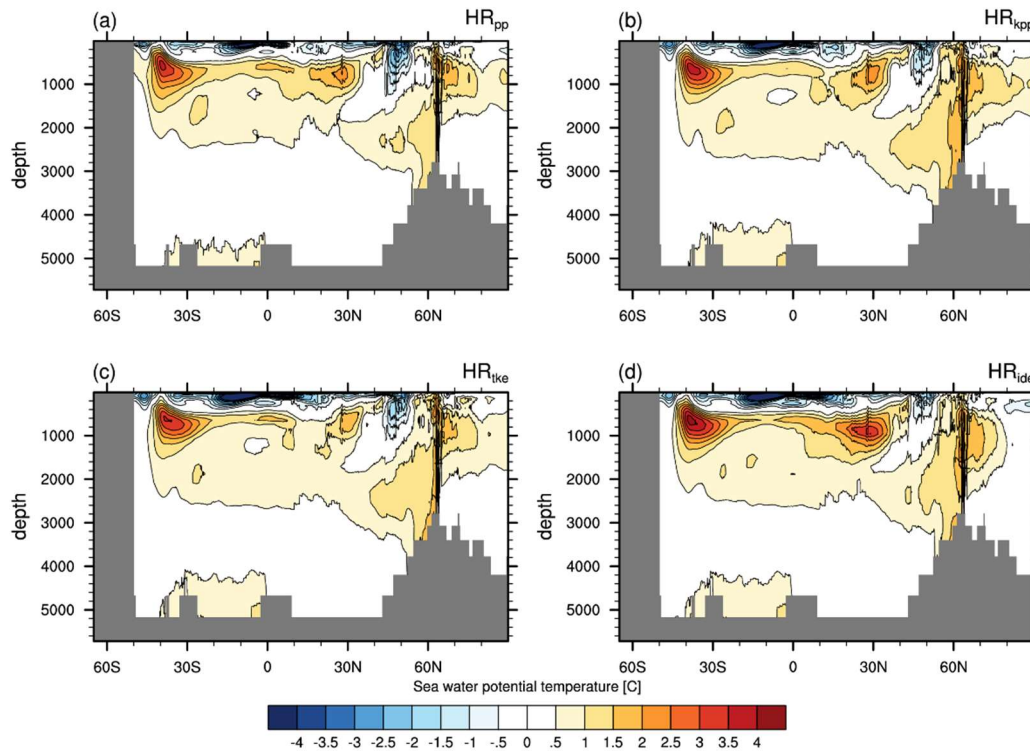


Figure 4: Zonal-mean bias of potential temperature to EN4 (1945-1955) in the Atlantic and Arctic Ocean for (a)  $HR_{pp}$ , (b)  $HR_{kpp}$ , (c)  $HR_{tke}$ , and (d)  $HR_{ide}$ .

In the next sections, we will discuss some of the areas where IDEMIX affects the model bias in  $HR_{ide}$ , both positively or negatively. We note, however, already here that the errors related to the model resolution govern the bias pattern and that the choice of vertical mixing scheme is only of second order.

### 3.1.3.3 Atlantic Water Layer in the Arctic Ocean and the circulation at Fram Strait

A well-known error of many state-of-the-art ocean models is a too thick and too deep Atlantic Water Layer (AWL) in the Arctic Ocean (e.g. Holloway et al., 2007, Shu et al., 2019). This error is thought to be related to model resolution and to vertical mixing schemes, in particular to the choice of the background mixing value (Zhang and Steele, 2007; Liang and Losch, 2018). In terms of model resolution, it was recently shown that a high-resolution ocean ( $1/10^\circ$  or better) reduces this bias (Wang et al., 2018; Gutjahr et al., 2019). Here, however, we demonstrate that the bias is also reduced by using an improved vertical mixing scheme (i.e. IDEMIX).

Warm and saline Atlantic Water (AW) is the main contributor of salt and oceanic heat transport into the Arctic Ocean. The AW flows northward first as the Norwegian Current in the Nordic seas until it splits into two branches south of Svalbard (Fig. 5). A small branch flows eastwards and enters the Barents Sea via the Barents Sea Opening and flows into the Arctic Ocean at the St. Anna Trough in the northern Kara Sea. The main branch continues northward as the West Spitsbergen Current (WSC). Most of the WSC recirculates south of Fram Strait (Southern Recirculation), thereby becoming a part of the East Greenland Current (EGC). Only a small fraction flows through Fram Strait into the Arctic Ocean, thereby supplying the AWL. The final passage of the WSC into the Arctic Ocean is at the Yermak Plateau (YP), a bathymetric feature north of Svalbard. Here the diverging isobaths split the WSC into three branches. The main fraction recirculates southwards between  $78^\circ\text{N}$  and  $80^\circ\text{N}$ , becoming part of the East Greenland Current. Only a small fraction continues northwards as the Svalbard branch, which flows along the upper inward continental slope of Svalbard at a depth of about 500m. Both currents are visible in Fig. 5. Below, at a depth of about 1000m, the Yermak branch flows along the margin of the YP as a boundary current (e.g. Crews et al., 2017). The Yermak branch is only weakly present in  $\text{HR}_{\text{ide}}$  (not shown). In fact, an unrealistic flow emerges in  $\text{HR}_{\text{pp}}$ ,  $\text{HR}_{\text{kpp}}$  and  $\text{HR}_{\text{tke}}$ , which flows in the opposite direction, i.e. south along the YP in the eastern Fram Strait. Although  $\text{HR}_{\text{ide}}$  produces no noticeable (northward flowing) Yermak branch, this unrealistic southward flow is not present. At the surface, heat is directly lost to the atmosphere, whereas at depth heat loss is attributed to turbulent mixing, induced by currents and internal waves, and to eddy activity (Fer et al., 2010). Based on measurements, the cooling of the WSC depends on whether it flows around or above the YP, which results in different mixing rates (Fer et al., 2010). The Svalbard and Yermak branches then flow along the shelf break to the east, where they encounter the Barents Sea branch at St. Anna Trough. Both water masses continue cyclonically thereafter as a boundary current around the Arctic Ocean.

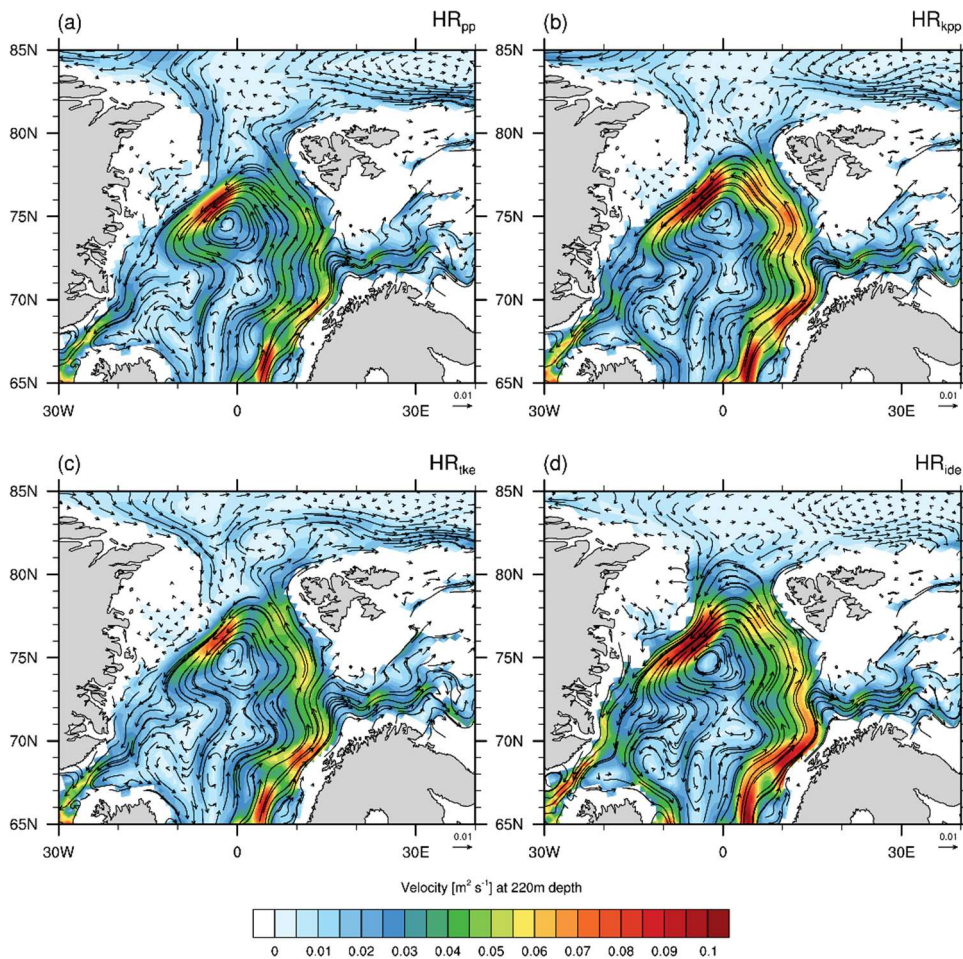


Figure 5: Circulation in the Nordic seas and at Fram Strait at a depth of 220m simulated by MPI-ESM1.2 (a) HR<sub>pp</sub>, (b) HR<sub>kpp</sub>, (c) HR<sub>tke</sub>, and (d) HR<sub>ide</sub>. Indicated by the arrow length at the bottom right is the reference velocity.

The first indication of why the AWL warm bias in HR<sub>ide</sub> is smaller (Fig. 6) appears to be related to a stronger recirculation, which splits only in HR<sub>ide</sub> into a Southern (south of 80°N) and a Northern Recirculation (north of 80°N). A stronger southward recirculation means less inflow of Atlantic Water to the north and east of Svalbard, so that less heat is carried into the Arctic Ocean through Fram Strait. This stronger return circulation might be related to enhanced deep convection in the Nordic seas (Fig. 9), which in turn accelerates the geostrophic flow around the convection centre due to steeper isopycnal gradients. In fact, the Greenland Sea gyre is up to 5 Sv stronger in HR<sub>ide</sub> (Fig. 9e). The Northern Recirculation further transfers volume and heat from the WSC to the EGC, which does not enter the Arctic Ocean. A similar circulation structure develops also in our eddy-resolving MPI-ESM1.2-ER model (Gutjahr et al., 2019, not shown), although with more sharply defined currents. We neglect here the effect of mesoscale eddies on the heat transport, as they are not resolved in the HR model because of the small Rossby radius at this high latitude.

In HR<sub>pp</sub>, HR<sub>kpp</sub>, and HR<sub>tke</sub> the warm bias of the AWL is about +2 to +3°C at YP and

approximately +1 to +2°C further downstream along the shelf break of the Eurasian Basin (Fig. 6). Some of the AW also crosses Lomonosov Ridge and spreads into the Markarov and Canada basins. In  $HR_{ide}$  there is only a warm bias at YP but not further downstream into the Arctic. This further indicates stronger mixing at YP, which is known to be a hot spot for internal wave activity and mixing (e.g. Fer et al., 2010). This enhanced mixing causes a stronger heat release to the atmosphere, which cools the continuing Atlantic Water more strongly than in the other simulations.

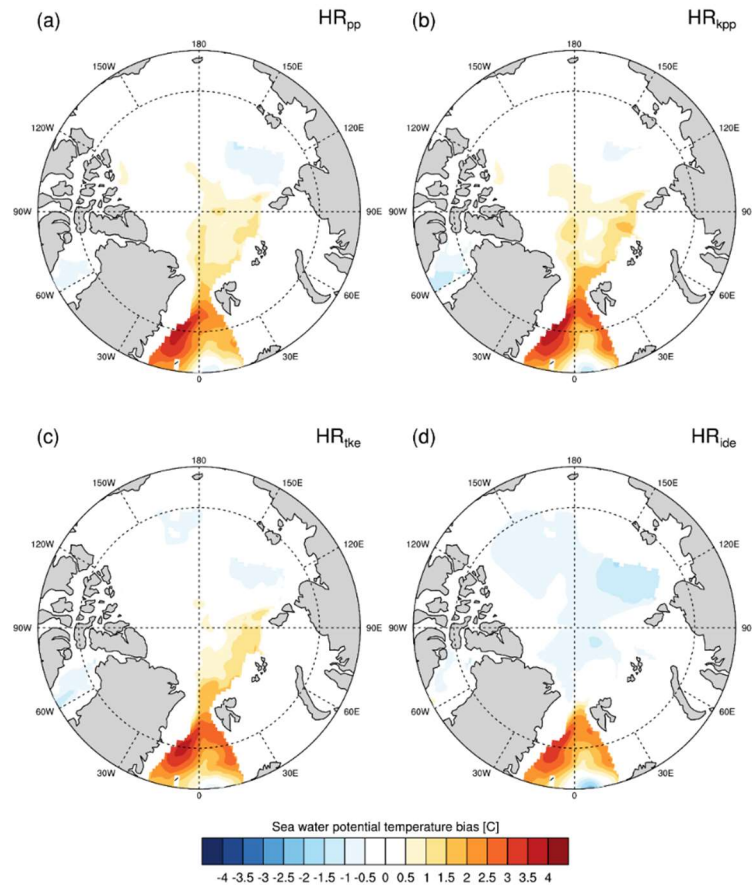


Figure 6: Temperature bias at 420m depth to EN4 for (a)  $HR_{pp}$ , (b)  $HR_{kpp}$ , (c)  $HR_{tke}$ , and (d)  $HR_{ide}$ .

A comparison of  $K$  at 690m depth at Fram Strait and in the Arctic Ocean (Fig. 7) reveals two important differences in  $HR_{ide}$ . First, the mixing near YP is slightly stronger in  $HR_{ide}$  (Fig. 7d), supporting the assumption of increased heat release. In fact, the sensible heat flux is about 20 to 40  $Wm^{-2}$  larger in  $HR_{ide}$  than in  $HR_{pp}$  (not shown). For comparison, the sensible heat flux is only about 10 to 20  $Wm^{-2}$  stronger in  $HR_{kpp}$  and  $HR_{tke}$ . However, the heat loss, in particular the sensible heat flux, is already stronger in the Greenland Sea (further densifying the water for deep convection) and the temperature of the Atlantic Water is already about 1°C colder in  $HR_{ide}$  at Fram Strait. This explains why the heat flow towards Fram Strait is less in  $HR_{ide}$ , even though the Greenland Sea Gyre is stronger and thus warmer AW could be expected (Chatterjee et al., 2018).

The other obvious difference in  $HR_{ide}$  is a much-reduced vertical mixing in the interior Arctic

Ocean, away from the shelf break of the Eurasian basin. The mixing coefficient  $K$  is at the background value ( $1.05^{-5} \text{m}^2 \text{s}^{-1}$ ) in  $\text{HR}_{\text{pp}}$  and  $\text{HR}_{\text{kpp}}$ , and of a similar order in  $\text{HR}_{\text{tke}}$ . In contrast,  $K$  in  $\text{HR}_{\text{ide}}$  is one order lower,  $O(10^{-6} \text{m}^2 \text{s}^{-1})$ , and in the Canadian Basin even two orders lower, which better agrees with microstructure measurements (Fer, 2009). The interior Arctic Ocean is isolated by sea ice from the atmosphere, so that wind stress is a minor source for mixing in all simulations. In addition, brine rejection is less effective as a mixing mechanism because of the strong vertical salinity gradients. Since we do not parameterize double diffusion, a main source for mixing is thus lateral intrusion. A problem arises, however, by assuming a constant background mixing value, or, in other words, that internal waves break in the interior Arctic as they do in other ocean basins.

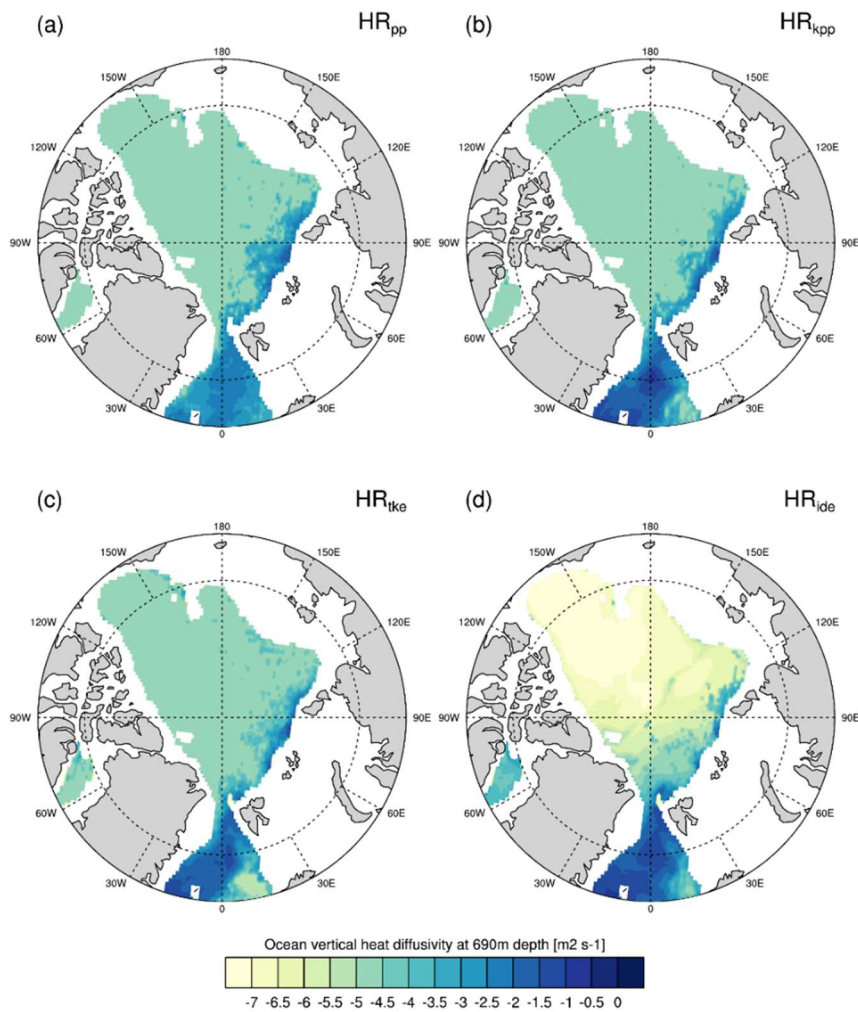


Figure 7: Time-averaged vertical diffusivity coefficient  $\log_{10}(K)$  ( $\text{m}^2 \text{s}^{-1}$ ) in the Arctic Ocean at a depth of 690 m in the MPI-ESM1.2-HR simulations for (a)  $\text{HR}_{\text{pp}}$ , (b)  $\text{HR}_{\text{kpp}}$ , (c)  $\text{HR}_{\text{tke}}$ , and (d)  $\text{HR}_{\text{ide}}$ .

In fact, internal waves are trapped at the place of their origin and do not propagate far into the Arctic Ocean. This trapping occurs because the Arctic Ocean is north of the critical latitude, which is  $74.5^\circ \text{N}$  for the  $\text{M}_2$  tide, beyond which the Earth's rotation prohibits freely propagating internal waves. As a result, they dissipate at or very close to their source region with properties similar to lee waves (Rippeth et al., 2015, Rippeth et al., 2017). Thus, there is no contribution

to small-scale turbulence in the interior Arctic Ocean, so that the mixing coefficient becomes very low in  $HR_{ide}$ . An example where higher mixing above topography is visible in the interior Arctic Ocean is a sharply defined band of higher  $K$  along the Lomonosov ridge in Fig. 7d. Here internal waves immediately dissipate after their generation.

All simulations show high mixing coefficients along the shelf break in relation to the cyclonically spreading AW. A local maximum is simulated where the Barents Sea Water encounters the AW from Fram Strait at the St. Anna Trough in the Kara Sea. However, the mixing is somewhat lower in  $HR_{ide}$ , with also lower velocities once the Barents Sea Water branch has entered the Nansen Basin.

### 3.1.3.4 Subpolar North Atlantic and the Nordic seas

The subpolar North Atlantic (SPNA) and the Nordic seas are important regions for the global climate where the vertical link of the upper warm and lower cold branch of the Meridional Overflow circulation is accomplished. The northward flowing warm Atlantic water is cooled due to extensive heat loss to the atmosphere until it becomes dense enough to sink to deeper layers and leaves the SPNA with the southward Deep Western Boundary Current.

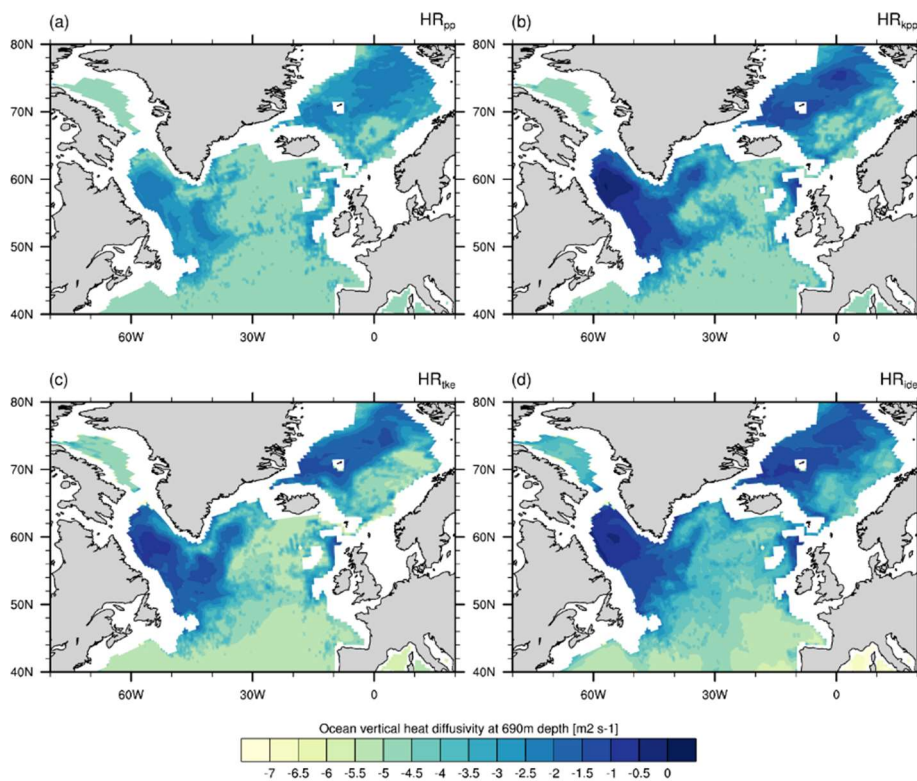


Figure 8: Time-averaged vertical diffusivity coefficient  $\log_{10}(K)$  ( $m^2 s^{-1}$ ) at a depth of 690 m in the MPI-ESM1.2-HR simulations for (a)  $HR_{pp}$ , (b)  $HR_{kpp}$ , (c)  $HR_{tke}$ , and (d)  $HR_{ide}$ .

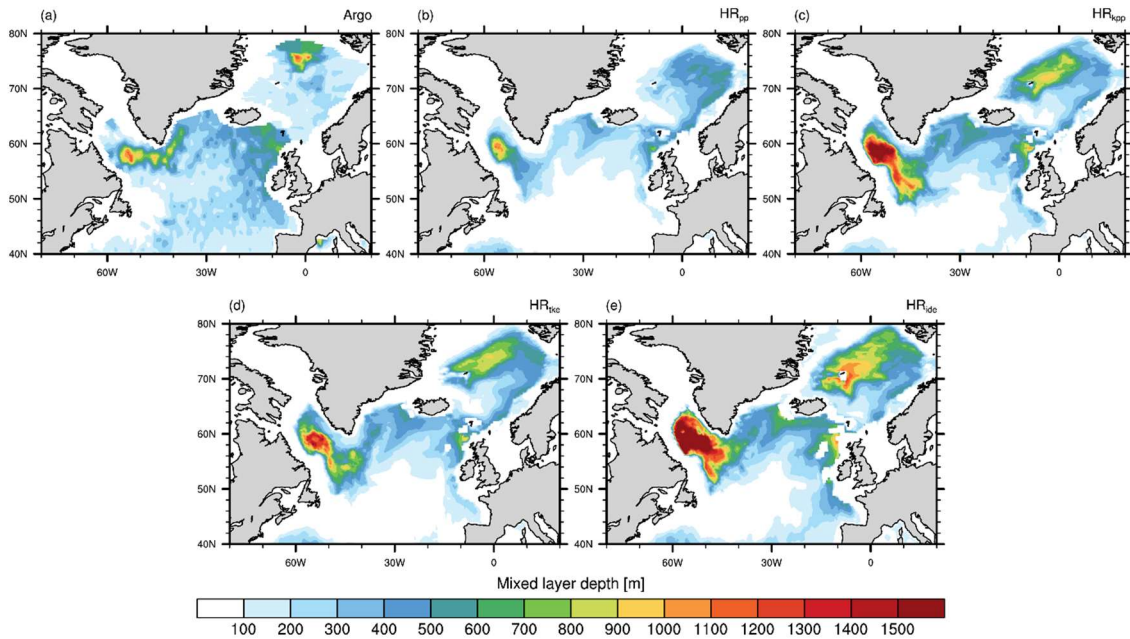


Figure 9: Time-averaged mixed layer depths (m) in March calculated (a) from  $1^\circ \times 1^\circ$  Argo float data (Holte et al., 2017) from January 2000 to April 2018 by the density threshold method ( $\sigma_t = 0.03 \text{ kg m}^{-3}$ ) and with  $\sigma_t = 0.01 \text{ kg m}^{-3}$  from MPI-ESM1.2 (b) HR<sub>pp</sub>, (c) HR<sub>kpp</sub>, (d) HR<sub>tke</sub>, and (e) HR<sub>ide</sub>.

The sinking of these dense water masses results from downwelling along the boundary current in the SPNA and from open ocean deep convection. The SPNA and the GIN (Greenland-Iceland-Norwegian) seas are one of the few places where open-ocean deep convection occurs. Convection, or vertical instability, is parameterised differently in the vertical mixing schemes, so that we expect also differences in the vertical diffusion and the mixed layer depths (MLDs).

The vertical diffusion  $K$  at 690 m depth is shown in Fig. 8 to illustrate some differences resulting from the different mixing schemes. First, we notice that all simulations show the largest values of  $K$  in the Labrador Sea and in the GIN seas. In the sensitivity simulations (Fig.8b-d), the diffusivity is considerably larger than in the reference simulation. In particular, we note enhanced vertical mixing in the Irminger Sea, which has become acknowledged by recent studies as a deep convection area (e.g. Pickart et al., 2003; Våge et al., 2011) that contributes to the Labrador Sea Water (LSW) formation.

In HR<sub>pp</sub> vertical instability is parameterized by enhancing the diffusivity to  $K = 0.1 \text{ m}^2\text{s}^{-1}$ . In HR<sub>kpp</sub>, convection is parameterised as non-local transport terms, which redistribute the surface fluxes throughout the boundary layer. These non-local transport terms depend on the net heat and net freshwater fluxes at the ocean surface, on  $K$ , and on a dimensionless vertical shape function (Large et al., 1994; Griffies et al., 2013). In HR<sub>tke</sub> and in HR<sub>ide</sub> the buoyancy term (third term on the right-hand side of Eq. (2)), which usually destroys TKE through stratification, becomes a source term for TKE in the case of negative  $N^2$  (unstable stratification). However, besides differences in the parameterisations, remotely changed water mass properties also affect convection and the MLD (Mixed Layer Depth) in the SPNA. Therefore, it is not straightforward to diagnose what is cause and what is consequence for

changes in the MLDs.

The average MLDs in March are shown in Fig. 9. Although we have to consider the different density thresholds that are used for Argo data, and that our simulations are 1950 control simulations, we find profound differences to Argo and across the simulations. In general,  $HR_{kpp}$ ,  $HR_{tke}$ , and  $HR_{ide}$  all tend to simulate deeper mixed layers in the SPNA, compared to  $HR_{pp}$ . All simulations show the deepest mixed layers in the Labrador Sea and a second maximum in the GIN seas. In the Labrador Sea, deep MLDs extend too far south in the direction of the so called Northwest corner and also too far north, because of the missing warm-core mesoscale eddies that would hamper convection and restratify the water column (e.g. Eden and Böning, 2002, Brüggemann et al., 2019, Gutjahr et al., 2019).

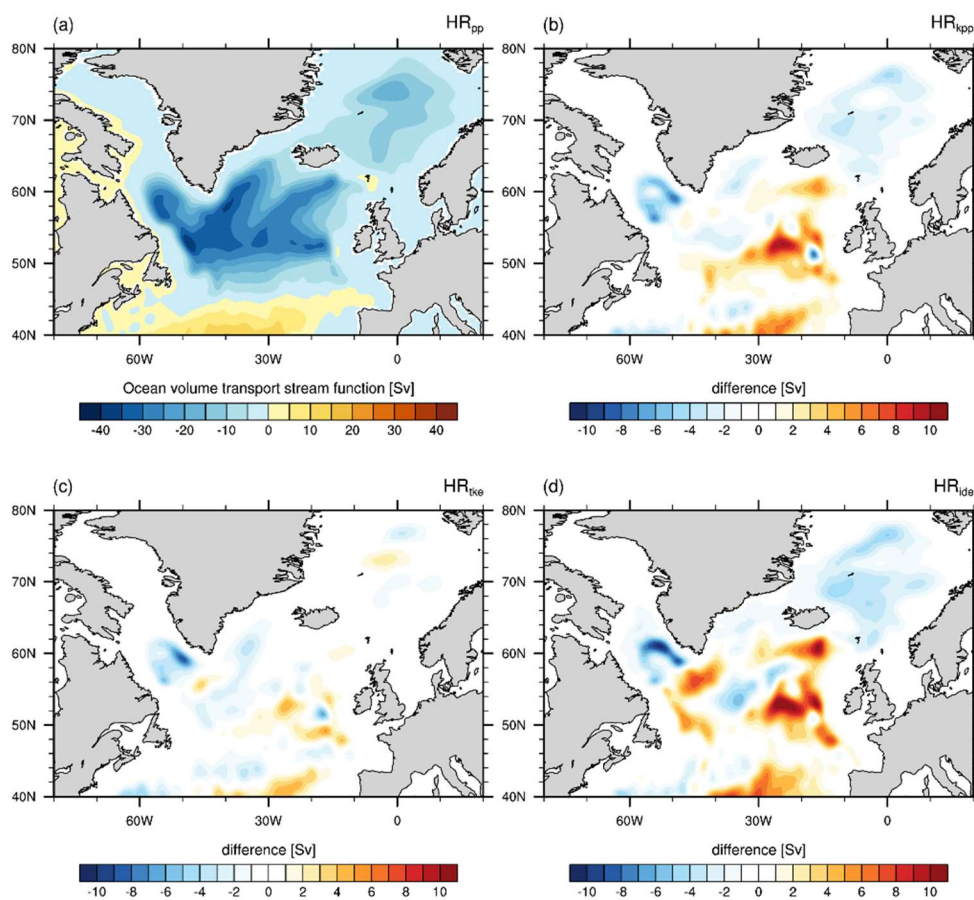


Figure 10: Time-averaged barotropic volume transport function for (a)  $HR_{pp}$ , and the differences (b)  $HR_{kpp} - HR_{pp}$ , (c)  $HR_{tke} - HR_{pp}$ , and (d)  $HR_{ide} - HR_{pp}$ .

$HR_{ide}$  simulates deeper mixed layers in the Greenland Sea, in particular around Jan Mayen. The latter might be due to internal wave activity in that area, in particular along the Kolbeinsey and Mohn Ridge and along the Jan Mayen Fracture Zone. The boundary current in the GIN seas is about  $0.5\text{ }^{\circ}\text{C}$  colder in  $HR_{ide}$  (not shown) and the Lofoten Basin Eddy, the area of the strongest heat release, is about  $1\text{ }^{\circ}\text{C}$  colder than in  $HR_{pp}$  (which is a bias of  $-2\text{ }^{\circ}\text{C}$  compared to EN4). In addition, salinity is roughly about  $0.2\text{ psu}$  higher in the GIN seas in  $HR_{ide}$  (also in  $HR_{tke}$  and  $HR_{kpp}$ ). These slightly colder but more saline water masses provide more favourable conditions

for deep convection in the GIN seas.

If a mixing scheme other than PP is used, the position of the marginal sea ice zone (15% sea ice concentration) in the northern seas is more consistent with satellite observations.

As already mentioned above, the geostrophic flow around the convection centres increases in response to enhanced convection, e.g. in the Labrador or Greenland Sea (Fig. 10b-d). This enhanced flow in turn steepens the isopycnals, thereby bringing weakly stratified water towards the surface (not shown) that further destabilizes the water column and preconditions it for convection.

On the other hand, there is also a stronger northward transport of volume and heat in  $HR_{kpp}$ ,  $HR_{tke}$  and  $HR_{ide}$ . The barotropic stream function of the AMOC is shown in Fig.11. Compared to  $HR_{pp}$ , all simulations produce a stronger upper cell, with a maximum  $>18$  Sv, which is also deeper reaching. While a stronger upper cell implies a stronger northward heat transport, a deeper upper cell indicates a stronger southward transport of North Atlantic Deep Water (NADW). We note, however, that the bottom cell is weaker in all sensitivity simulations compared to the reference simulation. Although IDEMIX affects the water mass properties and deep convection in the SPNA, the effect on the AMOC is virtually the same as in the KPP or TKE experiments. However, over longer simulation periods (several centuries) the additional mixing from internal waves might affect the diapycnal diffusion of the upwelling deep water, e.g. in the Pacific.

### 3.1.4 Key Points and Conclusions

To a leading order, we conclude that the choice of the mixing scheme has a minor effect in terms of model biases. The biases related to the  $0.4^\circ$  resolution of the model (the TP04 grid) dominate most regions of the World's Ocean. In particular, in the Atlantic we notice biases of too warm and saline water masses originating from the Mediterranean Overflow and from the Agulhas Current System. The bias in these water masses can be traced from the Atlantic to the GIN and Nordic Seas and then further to the Arctic Ocean. Based on recent studies, however, we know that most of these biases diminish in our model if an eddy-resolving ocean resolution (at  $0.1^\circ$ ) is used, as in the MPI-ESM1.2-ER (Gutjahr et al., 2019).

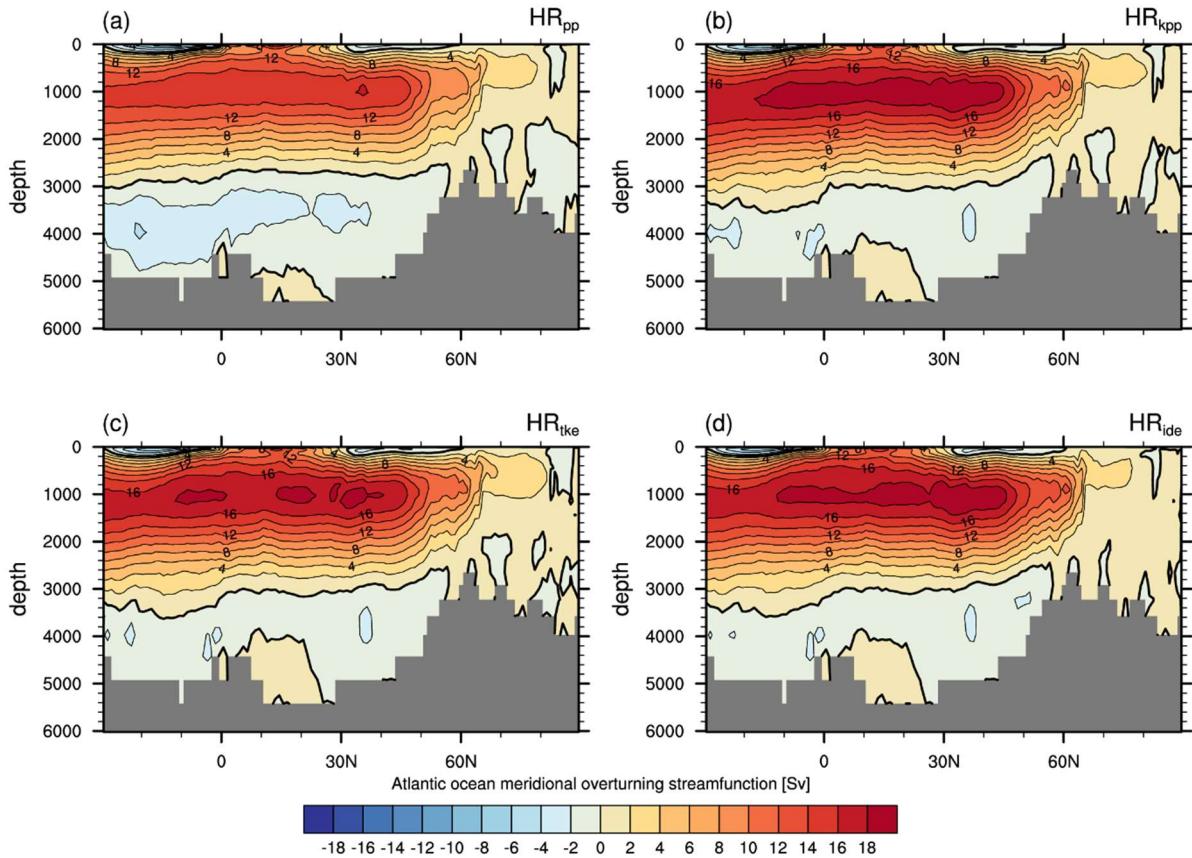


Figure 11: Eulerian stream function ( $Sv \cdot 10^6 \text{ m}^3 \text{ s}^{-1}$ ) of the AMOC in depth space for (a) HR<sub>pp</sub>, (b) HR<sub>kpp</sub>, (c) HR<sub>tke</sub>, and (d) HR<sub>ide</sub>.

However, we notice improvements by IDEMIX that reduce the bias to a similar extent as the eddy-resolving ocean does. The largest improvement in this respect is the improved circulation and mixing in the GIN Sea and at Fram Strait that reduces the warm bias of the Atlantic Water layer in the Arctic Ocean. Recently, it was shown that a high resolution, eddy-resolving ocean is needed in order to remove this bias (Wang et al., 2018; Gutjahr et al., 2019).

Our results demonstrate, however, that the prognostic simulation of internal wave energy and its dissipation is crucial to improve the Atlantic water layer temperatures in the Arctic Ocean. The reduction of this bias is not only important for the Arctic Ocean but might also impact the European climate, as the heat content of the Arctic Ocean influences the meridional temperature gradient and thus the westward wind strength in the Jet Stream.

## 3.2 The OSMOSIS OSBL scheme (NOC – George Nurser, Adrian New; Met Office - Catherine Guiavarc’h, Dan Copsey)

Much of the time, the turbulent motions in the ocean surface boundary layer (OSBL) are not given by classical shear turbulence. Instead they are in a regime known as ‘Langmuir turbulence’, dominated by an interaction between the currents and the Stokes drift of the surface waves (Belcher et al., 2012). The novel OSMOSIS parametrization of the ocean surface boundary layer (OSBL) aims to fully describe this ‘Langmuir regime’. The scheme uses flux-gradient relationships to parametrize the turbulent transports within the OSBL. These relationships have the same form as the non-local parametrizations used in the K-Profile Parametrization (KPP) scheme (Large et al., 1994), but are used for all variables and for the stable and unstable OSBL. The flux-gradient relationships are determined using results from large-eddy simulations. Other new features of the OSMOSIS scheme include the use of a prognostic equation to determine the depth of the OSBL, and the explicit representation of the stable pycnocline at the base of the OSBL.

In order to see whether it can improve ocean and climate model predictions, the OSMOSIS-OSBL scheme has been implemented and run in ocean-only NEMO runs at coarse ( $1^\circ$ ) and eddy-permitting ( $1/4^\circ$ ) resolution, and also in a short, coupled atmosphere (N96)–ocean ( $1/4^\circ$ ) run.

### 3.2.1 Description of the OSMOSIS OSBL scheme

We here provide a brief description of the scheme, noting that more complete details are available in Grant (2020). The model supposes a boundary layer of thickness  $h_{bl}$  enclosing a well-mixed layer of thickness  $h_{ml}$  and a relatively thin pycnocline at the base of thickness  $\Delta h$ . Fig. 12 shows typical (a) buoyancy structure and (b) turbulent buoyancy flux profile for the unstable boundary layer (losing buoyancy at the surface; e.g. cooling).

The pycnocline in the OSMOSIS scheme is assumed to have a finite thickness, and may include a number of model levels. This means that the OSMOSIS scheme must parametrize both the thickness of the pycnocline, and the turbulent fluxes within the pycnocline.

The OSMOSIS turbulent closure scheme is a similarity-scale scheme in the same spirit as the K-profile parameterization (KPP) scheme of Large et al. (1994).

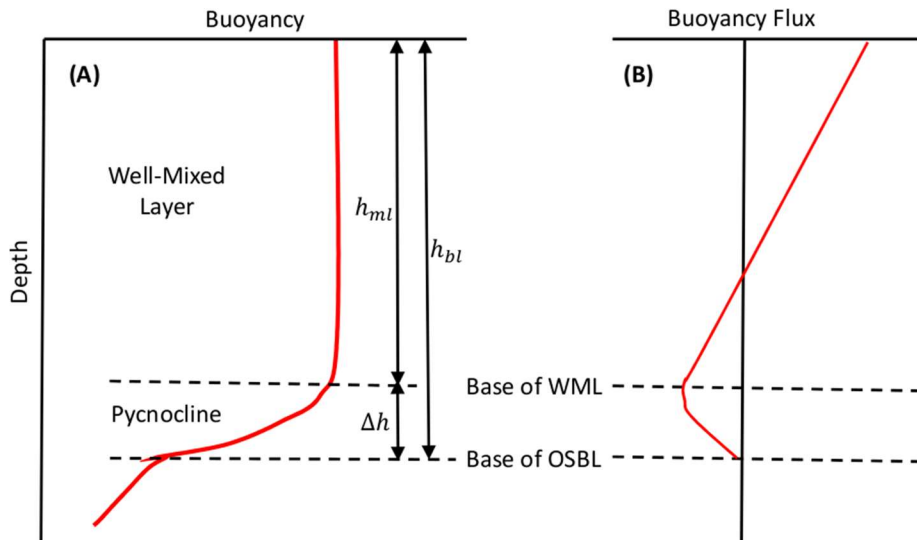


Figure 12: The structure of the entraining boundary layer. Profiles of (a) mean buoyancy (b) buoyancy flux.

A specified profile of diffusivity, scaled by the (OSBL) depth and a turbulent velocity scale, is imposed throughout the boundary layer  $-h_{bl} < z$ . Rather than the OSBL depth being diagnosed in terms of a bulk Richardson number criterion, as in KPP, it is set by a prognostic equation that is informed by energy budget considerations reminiscent of the classical mixed layer models of Kraus and Turner (1967). The model also includes an explicit parametrization of the structure of the pycnocline (the stratified region at the bottom of the OSBL). Presently, mixing below the OSBL is handled by the Richardson number-dependent mixing scheme used in Large et al. (1994).

### Velocity scales

Consideration of the power input by wind acting on the Stokes drift suggests that the Langmuir turbulence has the velocity scale:

$$w_{*L} = (u_*^2 u_{s0})^{1/3} \quad (3)$$

with  $u_*$  the surface friction velocity and  $u_{s0}$  the surface Stokes velocity, but at times the Stokes drift may be weak due to e.g. ice cover, short fetch, misalignment with the surface stress, etc. so a composite velocity scale is assumed for the stable (warming) boundary layer:

$$v_* = \left\{ u_*^3 \left[ 1 - \exp\left(-\frac{1}{2} \text{La}_t^2\right) \right] + w_{*L}^3 \right\}^{1/3}. \quad (4)$$

where  $\text{La}$  is the Langmuir number (see Grant, 2020 for more details). For the unstable boundary layer this is merged with the standard convective velocity scale  $w_{*C} = \left( \overline{w'b'_0} h_{ml} \right)^{1/3}$ , where  $\overline{w'b'_0}$  is the upwards surface buoyancy flux, to give:

$$\omega_* = \left( \nu_*^3 + 0.5 w_{*C}^3 \right)^{1/3}. \quad (5)$$

### ***The flux gradient model***

The flux-gradient relationships used in the OSMOSIS scheme take the form:

$$\overline{w' \chi'} = -K \frac{\partial \bar{\chi}}{\partial z} + N_{\chi,s} + N_{\chi,b} + N_{\chi,t}, \quad (6)$$

where  $\chi$  is a general variable and  $N_{\chi,s}$ ,  $N_{\chi,b}$  and  $N_{\chi,t}$  are the non-gradient terms, and represent the effects of the different terms in the turbulent flux-budget on the transport of  $\chi$ .  $N_{\chi,s}$  represents the effects that the Stokes shear has on the transport of  $\chi$ ,  $N_{\chi,b}$  is the effect of buoyancy, and  $N_{\chi,t}$  the effect of the turbulent transport. The same general form for the flux-gradient relationship is used to parametrize the transports of momentum, heat and salinity.

In terms of the non-dimensionalized depth variables

$$\sigma_{ml} = -z / h_{ml}; \sigma_{bl} = -z / h_{bl}, \quad (7)$$

and in unstable conditions, the eddy diffusivity  $K_d$  (and eddy viscosity  $K_v$ ) profiles are parametrized as:

$$K_d = 0.8 \omega_* h_{ml} \sigma_{ml} (1 - \beta_d \sigma_{ml})^{3/2} \quad (8)$$

$$K_v = 0.3 \omega_* h_{ml} \sigma_{ml} (1 - \beta_v \sigma_{ml}) \left(1 - \frac{1}{2} \sigma_{ml}^2\right) \quad (9)$$

where  $\beta_d$  and  $\beta_v$  are parameters that are determined by matching Eqs (8) and (9) to the eddy diffusivity and viscosity at the base of the well-mixed layer, given by

$$K_{d,ml} = K_{v,ml} = 0.16 \omega_* \Delta h \quad (10)$$

For stable conditions the eddy diffusivity/viscosity profiles are given by:

$$\begin{aligned} K_d &= 0.75 \nu_* h_{ml} \exp\left[-2.8 \left(h_{bl} / L_L\right)^2\right] \sigma_{ml} (1 - \sigma_{ml})^{3/2} \\ K_v &= 0.375 \nu_* h_{ml} \exp\left[-2.8 \left(h_{bl} / L_L\right)^2\right] \sigma_{ml} (1 - \sigma_{ml}) \left(1 - \frac{1}{2} \sigma_{ml}^2\right). \end{aligned} \quad (11)$$

The shape of the eddy viscosity and diffusivity profiles is the same as the shape in the unstable OSBL. The eddy diffusivity/viscosity depends on the stability parameter  $h_{bl} / L_L$  where  $L_L$  is analogous to the Obukhov length, but for Langmuir turbulence:

$$L_L = -w_{*L}^3 / \langle \overline{w'b'} \rangle_L, \square \quad (12)$$

with the mean turbulent buoyancy flux averaged over the boundary layer given in terms of its surface value  $\overline{w'b'}_0$  and (downwards) solar irradiance  $I(z)$  by

$$\langle \overline{w'b'} \rangle_L = \frac{1}{2} \overline{w'b'}_0 - g\alpha_E \left[ \frac{1}{2}(I(0) + I(-h)) - \langle I \rangle \right]. \quad (13)$$

In unstable conditions, the eddy diffusivity and viscosity depend on stability through the velocity scale  $w_*$ , which depends on the two velocity scales  $v_*$  and  $w_{*C}$ .

Details of the non-gradient terms in and of the fluxes within the pycnocline  $-h_{bl} < z < h_{ml}$  can be found in Grant (2020).

### ***Evolution of the boundary layer depth***

The prognostic equation for the depth of the neutral/unstable boundary layer is given by Grant (2020):

$$\frac{\partial h_{bl}}{\partial t} = W_b - \frac{\overline{w'b'}_{ent}}{\Delta B_{bl}} \quad (14)$$

where  $h_{bl}$  is the horizontally-varying depth of the OSBL,  $W_b$  is the mean vertical velocity at the base of the OSBL,  $\overline{w'b'}_{ent}$  is the buoyancy flux due to entrainment and  $\Delta B_{bl}$  is the difference between the buoyancy averaged over the depth of the OSBL (i.e. including the ML and pycnocline) and the buoyancy just below the base of the OSBL. This equation is for the case when the pycnocline has a finite thickness, and is based on the potential energy budget of the OSBL. It is the leading term in Grant et al. (2020) of a generalization of that used in mixed-layer models e.g. Kraus and Turner (1967) in which the thickness of the pycnocline is taken to be zero.

The entrainment flux for the combination of convective and Langmuir turbulence is given by:

$$\overline{w'b'}_{ent} = -\alpha_B \overline{w'b'}_0 - \alpha_S \frac{u_*^3}{h_{ml}} + G(\delta/h_{ml}) \left[ \alpha_S e^{-1.5La_t} - \alpha_L \frac{w_{*L}^3}{h_{ml}} \right] \quad (15)$$

where the factor  $G \equiv 1 - e^{-25\delta/h_{bl}}(1 - 4\delta/h_{bl})$  models the lesser efficiency of Langmuir mixing when the boundary-layer depth is much greater than the Stokes depth, and  $\alpha_B$ ,  $\alpha_S$  and  $\alpha_L$  depend on the ratio of the appropriate eddy turnover time to the inertial timescale  $f^{-1}$ . Results from LES modelling suggest  $\alpha_B = 0.18 F(fh_{bl}/w_{*C})$ ,  $\alpha_S = 0.15 F(fh_{bl}/u_*)$  and  $\alpha_L = 0.035 F(fh_{bl}/u_{*L})$ , where  $F(x) \equiv \tanh(x^{-1})^{0.69}$ .

For the stable boundary layer, the equation for the depth of the OSBL is:

$$\max\left(\Delta B_{bl}, \frac{w_{*L}^2}{h_{bl}}\right) \frac{\partial h_{bl}}{\partial t} = \left(0.06 + 0.52 \frac{h_{bl}}{L_L}\right) \frac{w_{*L}^3}{h_{bl}} + \overline{w'b'}_{>L}. \quad (16)$$

Equation (14) always leads to the depth of the entraining OSBL increasing (ignoring the effect of the mean vertical motion), but the change in the thickness of the stable OSBL given by Eq. (16) can be positive or negative, depending on the magnitudes of  $\overline{w'b'}_{>L}$  and  $h_{bl}/L_L$ . The rate at which the depth of the OSBL can decrease is limited by choosing an effective buoyancy  $w_{*L}^2/h_{bl}$ , in place of  $\Delta B_{bl}$  which will be  $\approx 0$  for the collapsing OSBL.

### ***Specification of Stokes drift***

The surface Stokes drift required to drive the model can either be specified (i) as proportional to the friction velocity of the wind, (ii) as that predicted by the steady saturated ‘wind-sea’ spectrum of Pierson and Moskowitz (1963) or (iii) explicitly from a wave model. The 1° ocean simulations run locally at NOC employ the explicit fields (iii), whereas the coupled and ¼° simulations use the wind-sea approximation (ii).

### **3.2.2 Model Implementation**

The OSMOSIS model been implemented into the NEMO code (r11653) of the trunk, closely aligned with NEMO v4.0.1, and is available on the Paris repository at: [https://forge.ipsl.jussieu.fr/nemo/browser/NEMO/branches/2019/dev\\_r11078\\_OSMOSIS\\_IMMERSE\\_Nurser](https://forge.ipsl.jussieu.fr/nemo/browser/NEMO/branches/2019/dev_r11078_OSMOSIS_IMMERSE_Nurser). This is the code that has been run locally in ocean simulations at NOC and is the development branch. There is also a version of the code that has been modified to operate with the specific UK Met O. GO8 NEMO ocean code setup: [https://forge.ipsl.jussieu.fr/ipsel/forge/projets/nemo/svn/NEMO/branches/UKMO/NEMO\\_4.0\\_OSMOSIS](https://forge.ipsl.jussieu.fr/ipsel/forge/projets/nemo/svn/NEMO/branches/UKMO/NEMO_4.0_OSMOSIS). This is the code that has been used to perform simulations at the Met. Office at ¼° ocean resolution for both ocean-only and coupled models.

### **3.2.3 Results**

A major problem with most current ocean and climate models is that there tends to be a warm bias in the Southern Ocean (SO) combined with Mixed Layer Depths (MLDs) that are often too shallow. We make this area a focus for the results below, but also pay attention to the performance of OSMOSIS in the North Atlantic.

#### ***3.2.3.1 Baseline 1°ocean-only CORE-II forced run***

The baseline NEMO run at 1° has been run locally on the NOC cluster, forced by the interannually varying CORE-II atmospheric dataset (Large and Yeager, 2009) for periods of up to 30 years. We first consider the results for Austral summer (February), taking averages for 3

model years (1986–1988). Note that, for consistency with the recent ARGO climatology of Holte et al. (2017), we specify MLD in terms of the criterion of Kara (2000) as the depth below the surface at which the density of the mixed-layer is an increment  $\Delta\rho$  greater than its value at 10m below the surface, with  $\Delta\rho = \rho_0\alpha\Delta T$  where  $\alpha$  is the expansion coefficient of water at the sea-surface salinity and temperature, and the temperature difference criterion  $\Delta T = 0.2^\circ\text{C}$ .

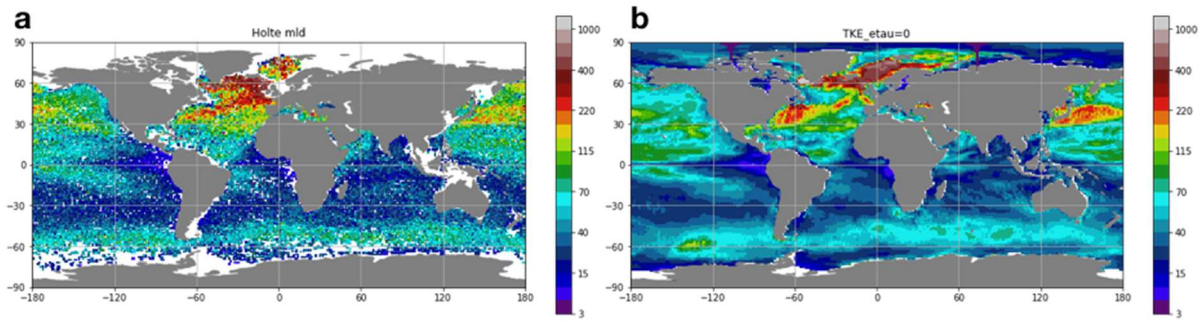


Figure 13: MLD in February from (a) ARGO climatology (Holte et al., 2017) and (b) as simulated at  $1^\circ$  resolution using the standard NEMO TKE model

Over the Antarctic Circumpolar Current (ACC) region ( $45^\circ$ – $60^\circ\text{S}$ ) the standard NEMO turbulent kinetic energy (TKE) model (Gaspar et al., 1990) gives summer mixed-layers that are on average too shallow and warm. This is evident both in previous coupled runs (where the Met O. coupled model HADGEM3 gave DJF (December-January-February) MLDs that were up to 80% too shallow; Belcher et al., 2012) and in our present  $1^\circ$  ocean-only runs. This is shown in Fig. 13a and b above where the green values (80–90m) in the climatology over the ACC are more typically cyan ( $<70\text{m}$ ) in the simulation. Currently this problem of too shallow summer mixed-layers is solved in NEMO by allowing part of the TKE within the surface mixed-layer to penetrate down into the transition zone immediately below the mixed layer—the so called `nn_etau=1` option (Madec et al., 2017: a parameterization of internal wave breaking). This is shown in the green line in Fig. 14a below, which is much closer to the observations than the orange line (the standard TKE model) - but this is really an engineering fix, tuned to give good results, without a plausible physical basis.

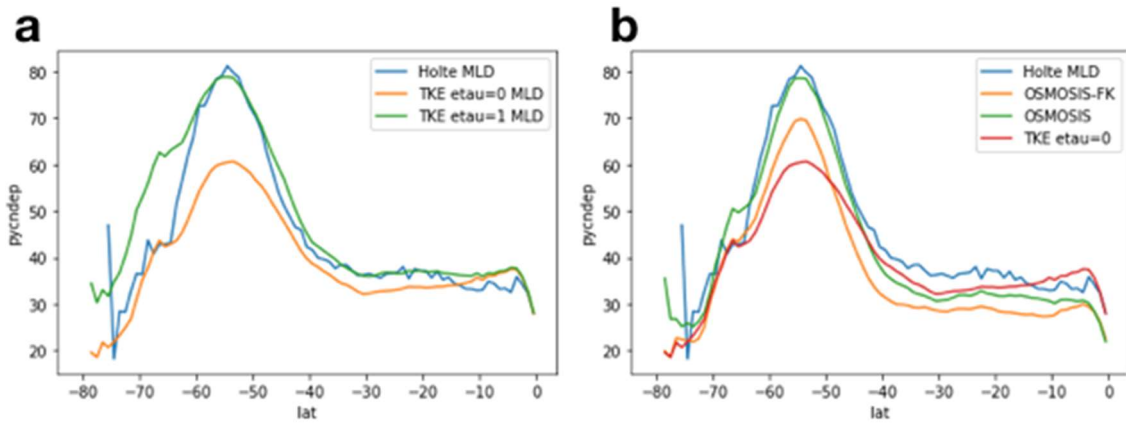


Figure 14: Variation with latitude of zonal-mean MLD in the SH (Southern Hemisphere) in February. (a) For the Holte climatology (blue line) and for the standard TKE model (orange line) and adjusted TKE model (green line); (b) For the standard OSMOSIS model (green line) the standard TKE model (red line) and the sub-mesoscale-aware OSMOSIS model (orange line: OSMOSIS coupled to the Fox-Kemper scheme, see below).

The Southern Ocean is a region where waves are strong and so the Langmuir circulations may be expected to drive additional mixing. The OSMOSIS OSBL model should therefore give more realistic, deeper, mixed-layer depths, and this is indeed the case; see Fig 14b, where the zonally-averaged OSMOSIS MLD (green) follows the observations very closely between 70°S and 45°S, and see also the OSMOSIS MLD field in Fig. 15a and b below, where there is a band of MLD ~85m deep along the ACC, sometimes too deep (e.g. at 120°W) and in other places too shallow (cf 180°W). Furthermore, the deeper band of MLDs in the OSMOSIS scheme as compared with TKE is easily seen by comparing Fig. 15a with Fig. 13b.

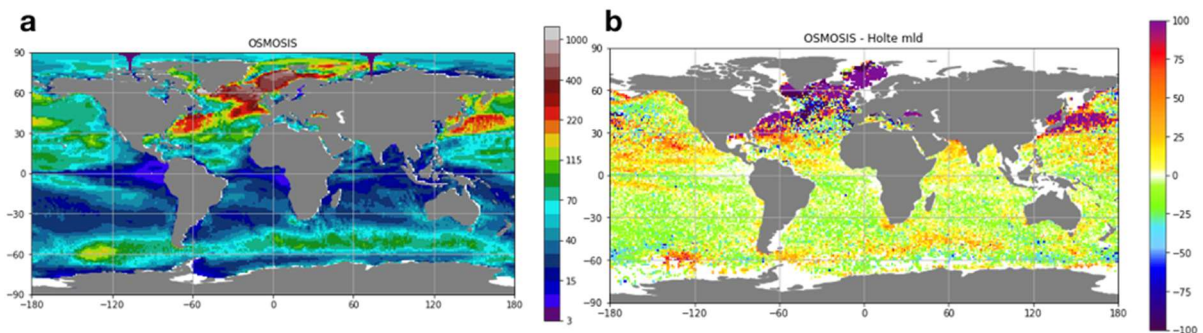


Figure 15: February MLD as simulated by NEMO with the OSMOSIS model. (a) MLD and (b) deviation from Holte climatology

Considering now the Sea-Surface Temperature (SST), both the TKE model and the OSMOSIS model tend to give SSTs that are too warm in Southern Ocean (SO) in the Austral summer (Fig. 16), but this excessive warmth results from other aspects of the model, probably mostly the poorly-known surface forcing. However, OSMOSIS gives slightly better (cooler) SO summer SSTs than the standard TKE model, as is evident in the zonal means (up to 0.2°; Fig. 17b).

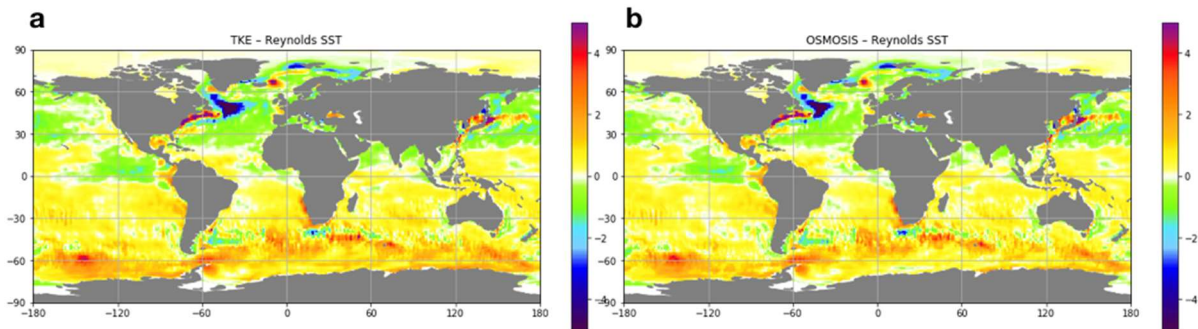


Figure 16: Deviations from Reynolds climatological February SST. (a) for standard ( $nn\_etau=0$ ) TKE model and (b) OSMOSIS

OSMOSIS also gives improved SSTs in the North Atlantic (NA) in February, as compared with the standard TKE scheme. This is evident in Fig. 16 which shows that the NA cold blob (the blue region in the western subpolar gyre between 45-60°N, which is another typical and major bias in such models) is significantly reduced, being less extensive towards the eastern subpolar gyre. This is further shown in Fig. 17b in which the zonal mean bias is reduced by about 0.3°C here. This could have beneficial consequences for climate modelling and prediction for Europe, but needs further examination in coupled models.

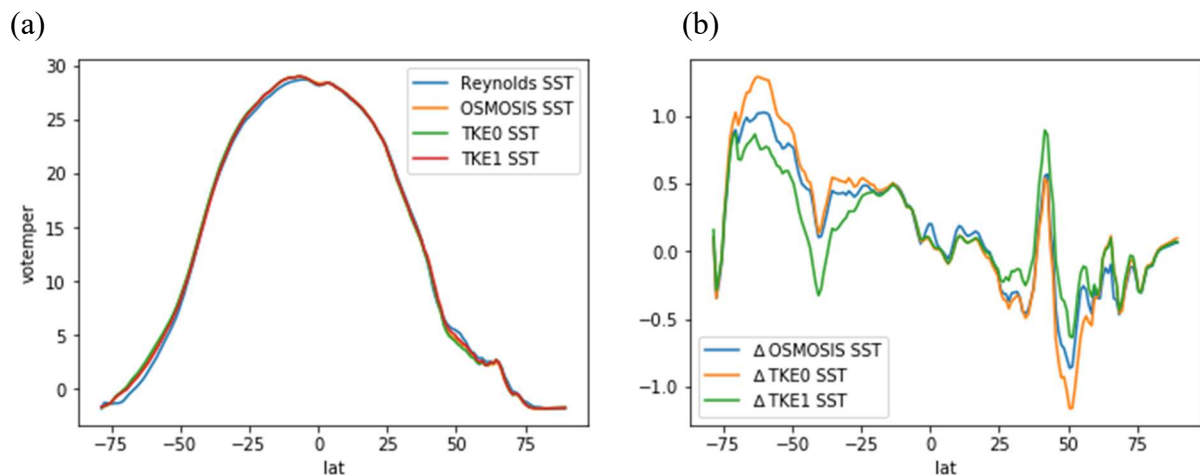


Figure 17: (a) February Zonal mean SSTs and (b) deviations from the Reynolds climatology for OSMOSIS, the standard TKE ( $nn\_etau=0$ , TKE0) and adjusted TKE ( $nn\_etau=1$ , TKE1).

The OSMOSIS model therefore performs well in the Southern Ocean summer, being better than the standard TKE scheme in terms of MLD and SST, and it also shows improved SSTs in the North Atlantic winter. However, as is evident from Fig. 15b, it gives February MLDs in the Northern Hemisphere that are substantially too deep.

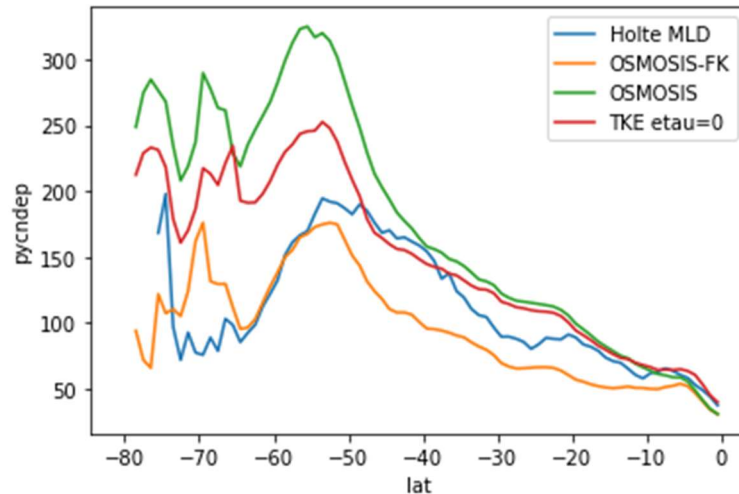


Figure 18: Zonally averaged MLDs in the Southern Hemisphere (SH) in August. Climatology (blue), OSMOSIS (green), standard TKE (red) and OSMOSIS-FK (orange).

These excessive winter MLDs are also evident in August (the Austral winter) in the Southern Hemisphere (Fig. 18). Note that the standard (i.e. no TKE below the ML) TKE model also shows excessive winter MLDs, so these excessive MLDs partly result from other model issues. But it remains the case that OSMOSIS-OSBL is giving too-deep winter mixed layers.

We believe that these excessive winter MLDs result from the fact that the OSMOSIS-OSBL model is set up to always entrain penetratively (with a density jump at the OSBL base) in winter situations of buoyancy loss and wind and wave energy supply. This is absolutely consistent with theory and Large-Eddy-Simulations (LES) of 1-D turbulent boundary layers. However, there is mounting observational evidence (e.g. Johnson et al., 2016), supported by extremely high-resolution models (e.g. the  $1/48^\circ$  global MITgcm: Siegelman, 2020; Torres et al., 2018), that in the real ocean the density jump at the base of the OSBL frequently disappears by mid-winter, and that turbulent transfer occurs through a weakly stratified layer below the surface well mixed-layer. This is thought (cf Boccaletti et al., 2007; Taylor and Ferrari, 2010; Fox-Kemper et al., 2011) to occur in association with sub-mesoscale motions that feed on the gravitational potential energy associated with lateral buoyancy gradients in the OSBL and produce vertical (upwards) buoyancy fluxes that tend to restratify the upper ocean. For reasonably deep mixed-layers, the TKE model is unable to maintain penetrative entrainment, largely due to its deficiencies in modelling TKE transport, and so will give more realistic (shallower) winter mixed-layers than the OSMOSIS-OSBL model. But these better mixed-layer depths result from fundamental inadequacies in the model.

The approach we have taken is to (i) closely couple OSMOSIS with the upwards vertical buoyancy fluxes associated with sub-mesoscale motions, as parametrized by Fox Kemper et al. (2008 a,b; 2011), so that the energy available to drive entrainment or maintain mixed-layer depth against surface buoyancy input in Eqs. (14) and (16) is reduced, and (ii) introduce a stratified transition layer beneath the surface mixed-layer. Preliminary results do indeed give

substantially shallower winter MLDs (see the orange line in Fig. 18), with more realistic results over the ACC in the Austral winter, but MLDs that are now too shallow in the subtropical gyres (and more generally in summer). Work is ongoing to lessen this excessive shallowing.

### 3.2.3.2 CORE-II forced ocean-only 1/4° runs

These runs were kindly performed with the GO8 NEMO ocean model - OSMOSIS branch by Dr. Catherine Guiavarc’h at the Met. Office. The comparison runs involve the TKE model with the engineering fix  $nn\_etau=1$  with the additional TKE flux below the ML.

Fig. 19 shows the MLDs for the two simulations in the Austral summer/ northern winter (DJF). As for the 1° case, the OSMOSIS run gives deeper summer MLs in the SO, here slightly deeper than observations (bottom right panel), while the modified TKE scheme is giving too-shallow MLs (bottom left panel). Again, OSMOSIS gives winter MLDs that are too deep in the N. Atlantic, as does the modified TKE scheme. OSMOSIS gives slightly deeper MLDs over the subtropical and eastern subpolar regions, but reduced (and improved) MLDs in the northern subpolar gyre (the blue region in the upper right panel of Fig. 19).

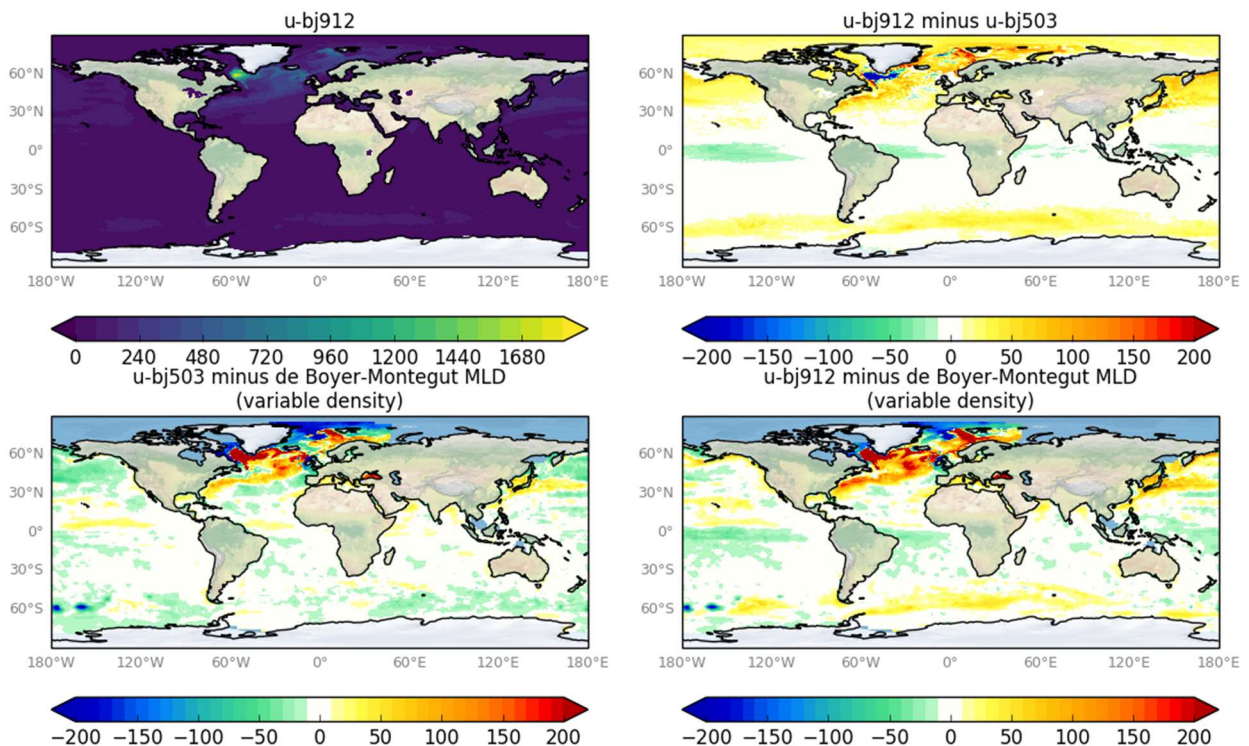


Figure 19: Met. O. CORE-II forced 1/4° ocean-only runs. Austral summer (DJF) MLD averages. Run u-bj912 is the OSMOSIS run and u-bj503 the comparison run with TKE (and  $nn\_etau=1$ ). The bottom two figures show the differences with the De Boyer-Montegut climatology.

In the Austral winter/ northern summer, similarly to the 1° results, northern hemisphere MLDs are good in both the OSMOSIS and TKE runs, while both TKE and OSMOSIS give too-deep MLDs over the ACC region (Fig. 20), with again OSMOSIS being particularly deep. Note that OSMOSIS MLDs are a little too shallow in equatorial regions.

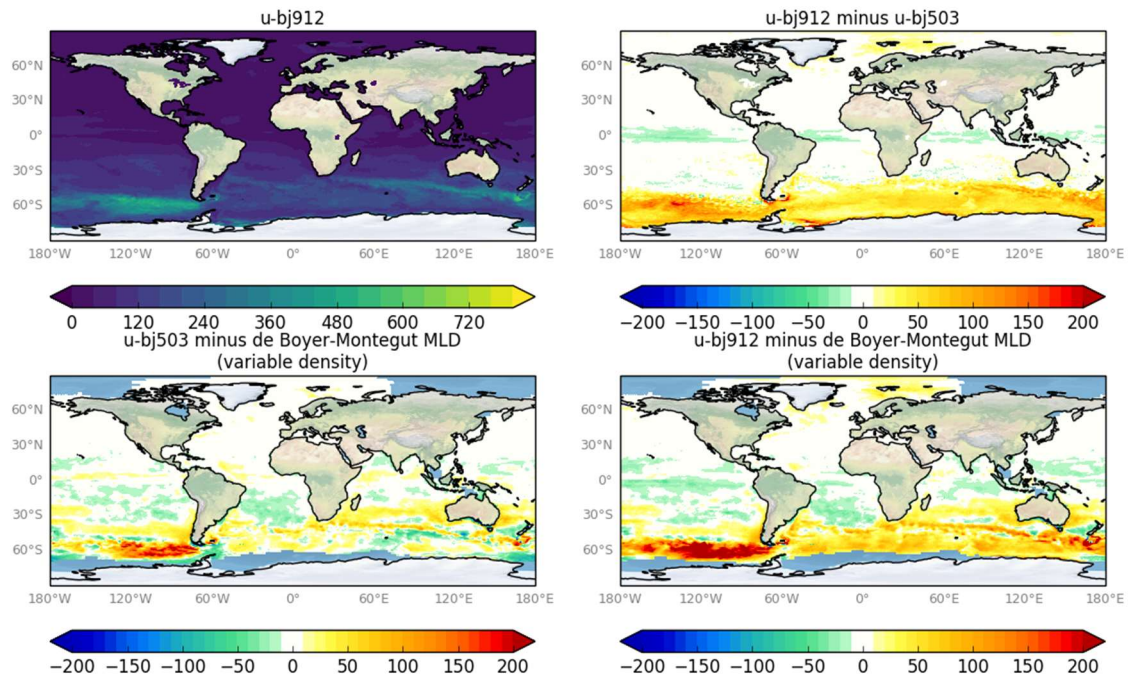


Figure 20. As Fig. 19 but for northern summer (average JJA) MLDs.

OSMOSIS southern-summer SSTs are warmer (see Fig. 21) than the already too-warm TKE SSTs in the Southern Ocean between 45°S and 30°S and polewards of 65°, but generally are slightly cooler and show less warm bias than those from the TKE run between 70°S and 45°S. This is in distinction to the results for the 1° case in which the TKE run with nn\_etau=1 is cooler than OSMOSIS in this region (Fig. 17) whereas now (at the higher resolution) OSMOSIS has the better SSTs.

Northern summer SSTs differ little between the OSMOSIS and TKE runs (Fig. 22).

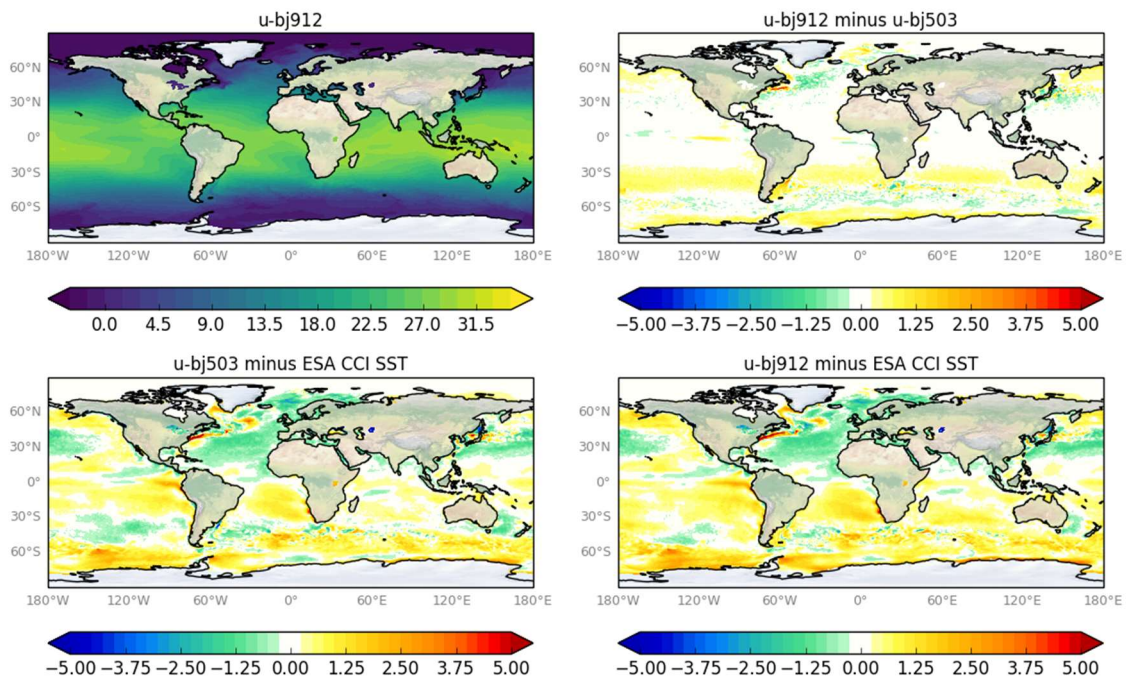


Figure 21. As for Fig. 19 but for Southern summer SST (average DJF), and now compared with the ESA CCI satellite SSTs.

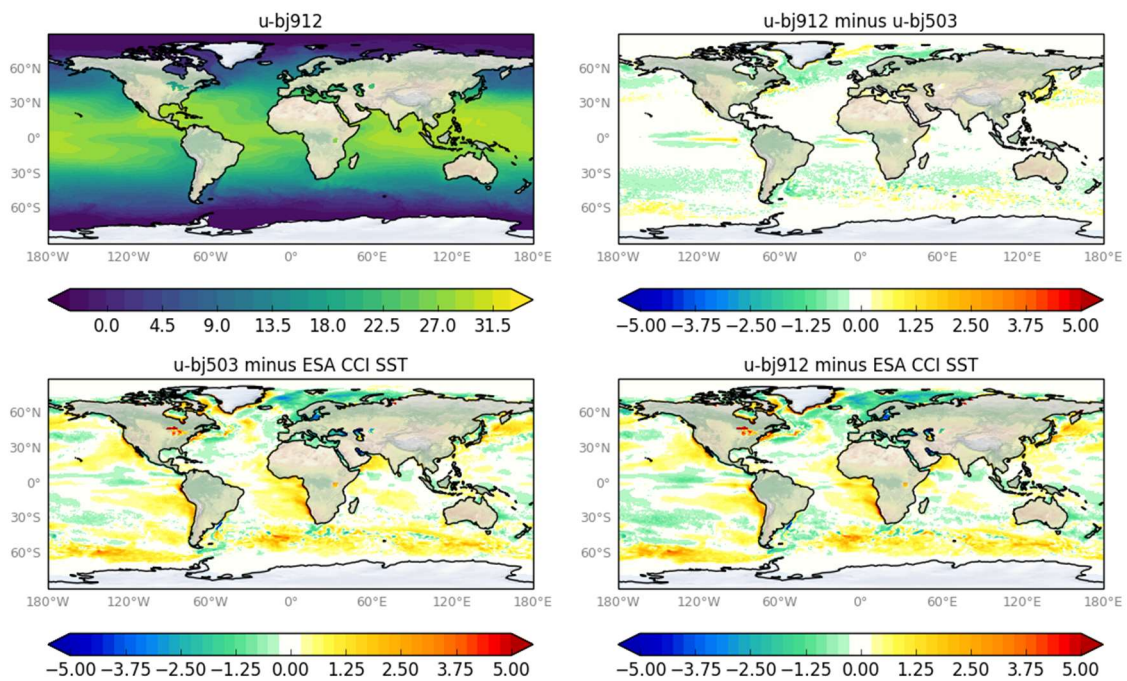


Figure 22. As Fig. 21 but for northern summer SST (average JJA).

### 3.2.3.3 Coupled simulations at $1/4^\circ$ ocean resolution

The OSMOSIS model was implemented in the ocean component of a short, coupled atmosphere (N96)–ocean ( $1/4^\circ$ ) and run for 10-years by Dr Dan Copsey at the UK Met. Office, using the same ocean code as the ocean-only  $1/4^\circ$  run described above. Results here show 10-yr averages of the run.

For this coupled run, southern-summer MLDs (Fig. 23) over the ACC agree well with climatology in the comparison TKE nn\_etau=1 run, but were anomalously deep with OSMOSIS, and again OSMOSIS MLDs were too shallow near the equator. Northern-summer MLDs (Fig. 24) are good for both OSMOSIS and TKE over the northern hemisphere, but too deep over the ACC in both runs, with OSMOSIS again deepest there and shallowest in equatorial regions. Southern-summer SSTs (Fig. 25) show most of the same biases in both runs (e.g. too-warm eastern southern tropical oceans and a generally too-cold North Atlantic) but are improved in OSMOSIS over the central ACC belt and made worse and further warmed in OSMOSIS in the southern subtropics and along the coast of Antarctica. Northern-summer SSTs (Fig. 26) are similar in the northern hemisphere, but the warm ACC bias of the TKE run is exacerbated with OSMOSIS.

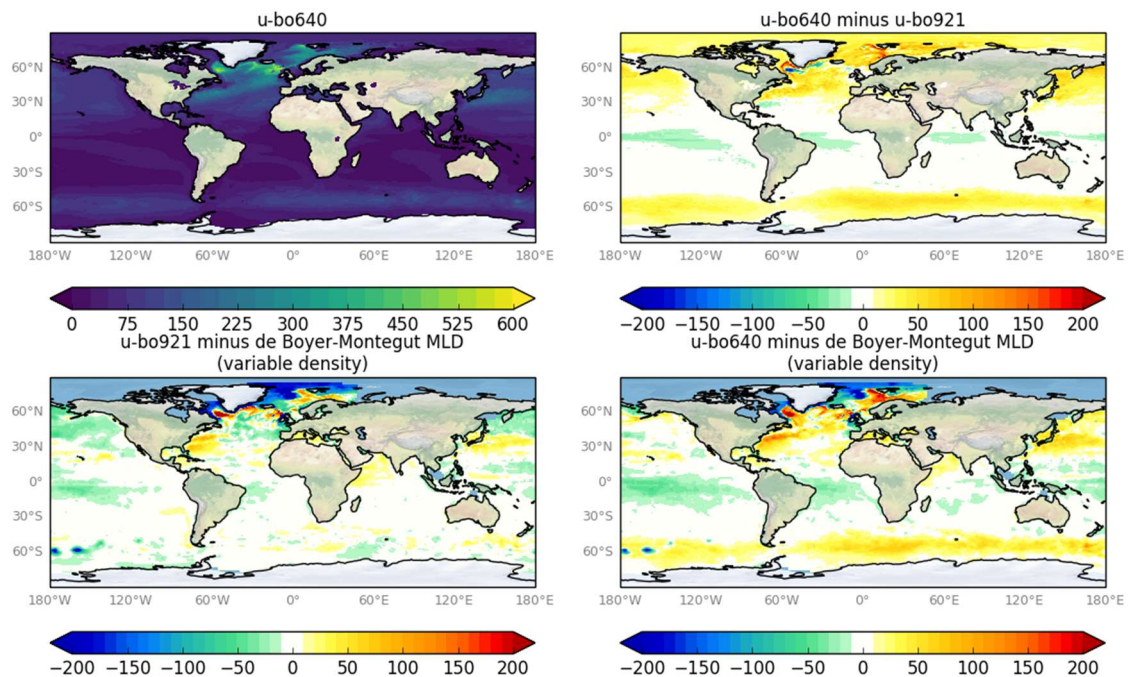


Figure 23. Southern summer (DJF) averages of MLD. Run u-bo640 is the coupled OSMOSIS run and u-bo921 the comparison run with TKE (and nn\_etau=1)

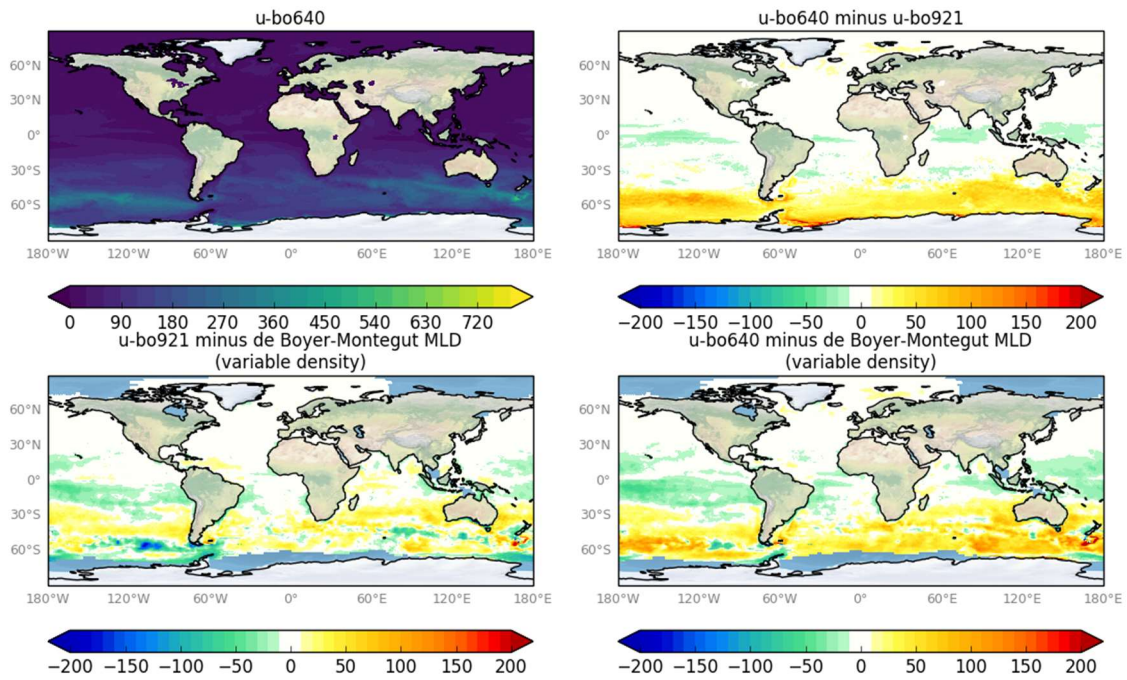


Figure 24. Northern summer (JJA averages) of MLD. Run u-bo640 is the OSMOSIS run and u-bo921 the comparison run with TKE (and nn\_etau=1).

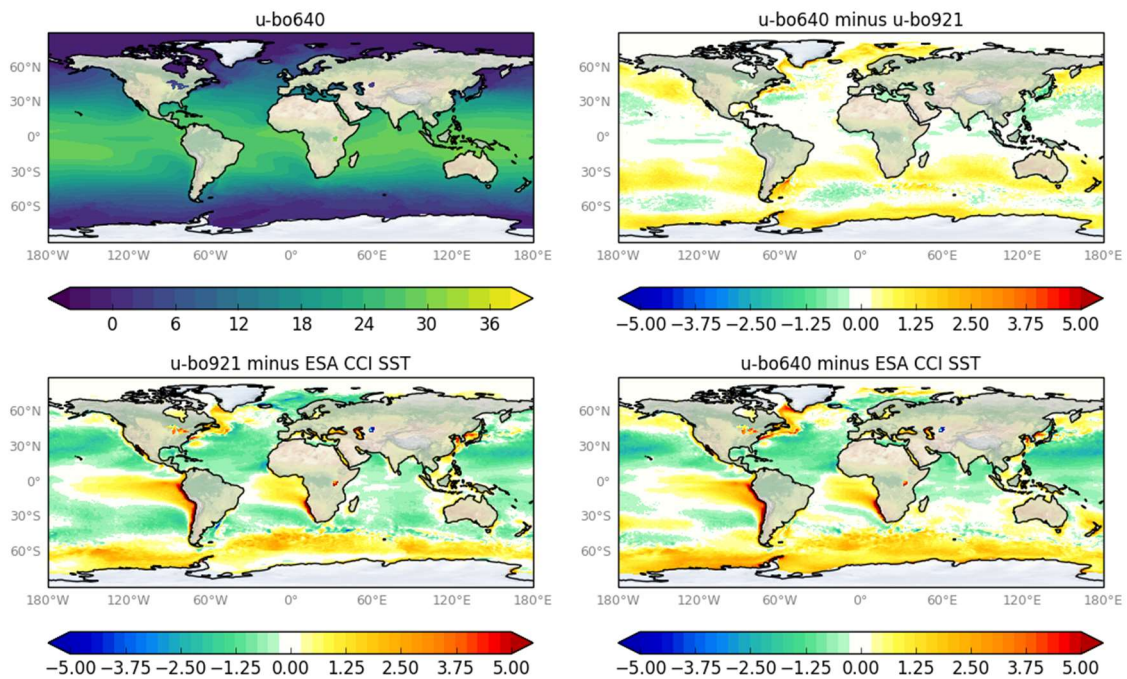


Figure 25. Southern summer (DJF) averages of SST for the coupled runs.

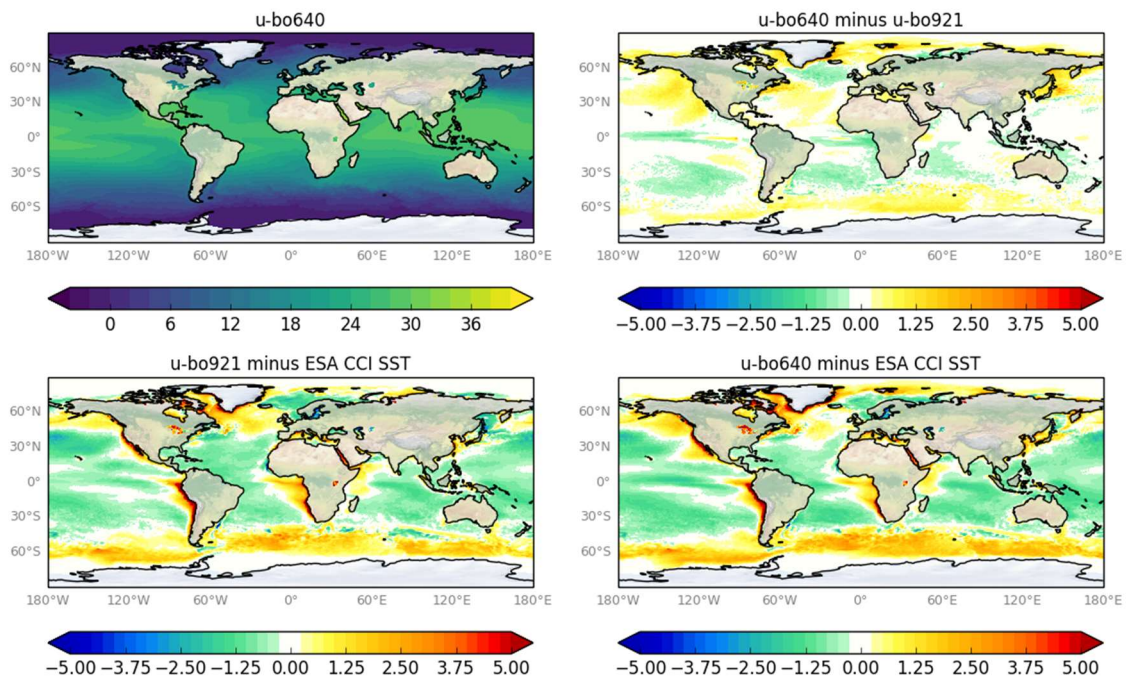


Figure 26. Northern summer (JJA) averages of SST for the coupled runs

### 3.2.4 Key Points and Conclusions

The new and innovative OSMOSIS OSBL parametrization has been implemented and run in the NEMOv4.0.1 ocean model at a range of resolutions, in both ocean-only and coupled configurations. Results show that it can produce adequately deep MLDs over the ACC in the southern summer, while the TKE model can only do this by using the physically dubious  $nn\_etau=1$  option whereby turbulent kinetic energy is artificially transferred beneath the OSBL. Additionally, there is some evidence that the OSMOSIS OSBL can reduce warm biases in the southern summer SSTs over the ACC. However, the OSMOSIS model generally gives winter MLDs that are too deep, especially over the ACC region. These results seem to hold broadly at both  $1^\circ$  and  $\frac{1}{4}^\circ$  resolution and in coupled and ocean-only simulations. However, note that the OSMOSIS OSBL has been developed and parameters set directly from large eddy simulations that give an idealized horizontally isotropic turbulence. There is considerable evidence that processes such as sub-mesoscale motions that feed off lateral large-scale buoyancy gradients act systematically to reduce winter mixed layer depths, and the modification to the OSMOSIS-OSBL scheme that links in the Fox-Kemper (FK) parameterization of these sub-mesoscale eddies is effective in reducing these winter deep ML biases, though further work is still needed to optimize the coupling between the two processes. Ultimately, the aim is to replace the TKE scheme with its unrealistic lack of deep penetrative convection which is also aided by an unrealistic parameterization of internal wave breaking below the mixed layer, by the OSMOSIS-FK scheme which includes both these physical effects

correctly. Considerable progress has been made towards this objective in PRIMAVERA, which therefore provides a framework for the inclusion of these realistic mixing processes in future generations of ocean and climate models.

#### **4. Lessons Learnt**

Overall, good progress was made towards including IDEMIX and OSMOSIS into the respective ocean models but this was slower than originally anticipated due to the complex nature of the schemes and their interactions with the other processes included in the models.

While IDEMIX was not developed solely at MPI during the course of PRIMAVERA, being already in use in other ocean models, it will be included in the official CVMix library (the Community Vertical Mixing Project, a suite of similar schemes for ocean models hosted in the US) following the PRIMAVERA work on this, and thereby will become available to many other modelling groups. Indeed, it is already in use in other modelling centres in Germany. Similarly, the OSMOSIS scheme was partly developed in other projects before PRIMAVERA, but as a result of PRIMAVERA it is now included in the main trunk of the NEMO model, so that it is now also useable by many other modelling groups worldwide. The development work on these schemes in PRIMAVERA will therefore leave a lasting legacy for future ocean and climate modelling studies.

#### **5. Links Built**

A strong link has now been built between MPI and NOC as a result of work on ocean mixing processes with OSMOSIS (in the upper ocean) and IDEMIX (in the deeper ocean). There is even a possibility that the schemes could be combined into a single scheme in the future. For IDEMIX, links have been strengthened with the US CVMix community and the connection will become even stronger in the future. From the OSMOSIS development, NOC has developed strong links with the University of Reading (Dr. A. Grant) and the Met Office (Prof. Stephen Belcher, and the JOMP team of model developers), and with the worldwide NEMO community through the inclusion of the scheme in the main model trunk. Further work on the scheme will also be undertaken within the EU IMMERSE project for NEMO development. The scheme may also be included in the H2020 NextGen project on water systems, and the DFG Transregio project on soil and vegetation.

## References

- Belcher, S. E., A. L. M. Grant, K. E. Hanley, B. Fox-Kemper, L. Van Roekel, P. P. Sullivan, W. G. Large, A. Brown, A. Hines, D. Calvert, A. Rutgersson, H. Pettersson, J.-R. Bidlot, P. A. E. M. Janssen, and J. A. Polton. A global perspective on Langmuir turbulence in the ocean surface boundary layer, *Geophys. Res. Lett.*, 39(18), doi:10.1029/2012GL052932, 2012.
- Blanke, B., and Delecluse, P.: Variability of the tropical Atlantic Ocean simulated by a general circulation model with two different mixed-layer physics. *J. Phys. Oceanogr.*, 23, 1363-1388, [https://doi.org/10.1175/1520-0485\(1993\)023<1363:VOTTAO>2.0.CO;2](https://doi.org/10.1175/1520-0485(1993)023<1363:VOTTAO>2.0.CO;2), 1993.
- Boccaletti, G., R. Ferrari, and B. Fox-Kemper. Mixed layer instabilities and restratification. *J. Phys. Oceanogr.*, 37(9):2228–2250, 2007.
- Brüggemann, N., Katsman, C.: Dynamics of downwelling in an eddying marginal sea: contrasting the Eulerian and the isopycnal perspective. *J. Phys. Oceanogr.*, <https://doi.org/10.1175/JPO-D-19-0090.1>, 2019.
- Chatterjee, S., Rai, R. P., Bertino, L., Skagseth, Ø., Ravichandran, M., Johannessen, O. M.: Role of Greenland Sea Gyre Circulation on Atlantic Water Temperature Variability in the Fram Strait. *Geophys. Res. Lett.*, 45, 8399-8406, <https://doi.org/10.1029/2018GL079174>, 2018.
- Crews, L., Sundfjord, A., Hatterman, T.: How the Yermak Pass Branch regulates Atlantic Water inflow to the Arctic Ocean. *J. Geophys. Res. Oceans*, 124, 267-280, <https://doi.org/10.1029/2018JC014476>, 2017.
- Czeschel, L., and Eden, C.: Internal wave radiation through surface mixed layer turbulence. *J. Phys. Oceanogr.*, 49, 1827-1844, <https://doi.org/JPO-D-18-0214.1>, 2019.
- Eden, C., Czeschel, L., Olbers, D.: Towards energetically consistent ocean models. *J. Phys. Oceanogr.*, 44, 3160-3184, <https://doi.org/10.1175/JPO-D-13-0260.1>, 2014.
- Eden, C. and Böning, C.: Sources of eddy kinetic energy in the Labrador Sea. *J. Phys. Oceanogr.*, 32, 3346-3363, [https://doi.org/10.1175/1520-0485\(2002\)032<3346:SOEKEI>2.0.CO;2](https://doi.org/10.1175/1520-0485(2002)032<3346:SOEKEI>2.0.CO;2), 2002.
- Fer, I.: Weak vertical diffusion allows maintenance of cold halocline in the central Arctic. *Atmospheric and Ocean Science Letters*, 2(3), 148-152, 2009.
- Fer, I., Skogseth, R., Geyer, F.: Internal Wave and Mixing in the Marginal Ice Zone near Yermack Plateau. *J. Phys. Oceanogr.*, 40, 1613-1630, <https://doi.org/10.1175/2010JPO4371.1>, 2010.
- Fox-Kemper, B., R. Ferrari, and R. Hallberg. Parameterization of mixed layer eddies. Part I: Theory and diagnosis. *J. Phys. Oceanogr.*, 38(6):1145–1165, 2008a.

Fox-Kemper, B. and R. Ferrari. Parameterization of mixed layer eddies. Part II: Prognosis and impact. *J. Phys. Oceanogr.*, 38(6):1166–1179, 2008b.

Fox-Kemper, B., G. Danabasoglu, R. Ferrari, S. M. Griffies, R. W. Hallberg, M. M. Holland, M. E. Maltrud, S. Peacock, and B. L. Samuels. Parameterization of mixed layer eddies. III: Implementation and impact in global ocean climate simulations. *Ocean Modell.*, 39(1–2):61–78, 2011.

Gaspar, P., Grégoris, Y., Lefevre, J.-M.: A simple eddy kinetic energy model for simulations of the oceanic vertical mixing: tests at station Papa and long-term upper ocean study site. *J. Geophys. Res. Oceans*, 95(C9), 16179-16193, <https://doi.org/10.1029/JC095iC09p16179>, 1990.

Good, S. A., Martin, M. J., Rayner, N. A.: EN4: quality controlled ocean temperature and salinity profiles and monthly objective analysis with uncertainty estimates. *J. Geophys. Res.*, 118, 6704-6716, <https://doi.org/10.1002/2013JC009067>, 2013.

Grant, A. L. M. The OSMOSIS scheme. In prep., 2020.

Griffies, S. M., Levy, M., Adcroft, A. J., Danabasoglu, R., Hallberg, R. W., Jacobsen, D., Large, W., Ringler, T. D.: Theory and numerics of the Community Ocean Vertical Mixing (CVMix) project, Tech. rep., available at <https://github.com/CVMix/CVMix-description>, 2013.

Gutjahr, O., Putrasahan, D., Lohmann, K., Jungclaus, J. H., von Storch, J.-S., Brüggemann, N., Haak, H., Stössel, A.: Max Planck Institute Earth System Model (MPI-ESM1.2) for the High-Resolution Model Intercomparison Project (HighResMIP), *Geosci. Model Dev.*, 12, 3241-3281, <https://doi.org/10.5194/gmd-12-3241-2019>, 2019.

Haarsma, R. J., M. J. Roberts, P.-L. Vidale et al. High Resolution Model Intercomparison Project (HighResMIP v 1.0) for CMIP6. *Geoscientific Model Development* 9 (11), 4185-4208, 2016.

Holloway, G., Dupont, F., Golubeva, E., Haekkinen, S., Hunke, E., Jin, M., Karcher, M., Kauker, F., Maltrud, M., Maqueda, M. A. M., Maslowski, W., Platov, G., Stark, D., Steele, M., Suzuki, T., Wang, J., Zhang, J.: Water properties and circulation in Arctic Ocean models, *J. Geophys. Res. Ocean*, 112, C04S03, <https://doi.org/10.1029/2006JC003642>, 2007.

Holte, J., L. D. Talley, J. Gilson, and D. Roemmich. An ARGO mixed layer climatology and database. *Geophysical Research Letters*, 44(11):5618–5626, 2017.

Jayne, S.: The impact of abyssal mixing parameterizations in an ocean general circulation model. *J. Phys. Oceanogr.*, 39, 1756–1775, <https://doi.org/10.1175/2009JPO4085.1>, 2009.

Jochum, M., Briegler, B. P., Danabasoglu, G., Large, W. G., Norton, N. J., Jayne, S. R., Alford, M. H., Bryan, F. O.: The impact of oceanic near-inertial waves on climate. *J. Clim.*, 26, 2833-2844, <https://doi.org/10.1175/JCLI-D-12-00181.1>, 2013.

Johnson, L., C. M. Lee, and E. A. D'Asaro. Global estimates of lateral springtime restratification. *Journal of Physical Oceanography*, 46(5):1555–1573, 2016/07/18, 2016.

Kara, A. B., P. A. Rochford, and H. E. Hurlburt. An optimal definition for ocean mixed layer depth. *J. Geophys. Res.-Oceans*, 105(C7):16803–16821, 2000.

Kraus, E.B. and J. Turner. A one dimensional model of the seasonal thermocline II. The general theory and its consequences. *Tellus*, 19, pp 98–106. doi: 10.1111/j.2153-3490.1967.tb01462.x, 1967.

Large, W. G., McWilliams, J. C., Doney, S. C.: Oceanic vertical mixing: a review and a model with a nonlocal boundary layer parameterization. *Rev. Geophys.*, 21, 363-493, <https://doi.org/10.1029/94RG01872>, 1994.

Large, W., and S. Yeager. The global climatology of an interannually varying air–sea flux data set, *Clim. Dynam.*, 33(2), 341–364. doi:10.1007/s00382-008-0441-3, 2009.

Liang, X., and Losch, M.: On the effects of increased vertical mixing on the Arctic Ocean and sea ice. *J. Geophys. Res. Oceans*, 123, 9266-9282, <https://doi.org/10.1029/2018JC014303>, 2018.

Madec, G., R. Bourdallé-Badie, P.-A. Bouttier, C. Bricaud, D. Bruciaferri, D. Calvert, J. Chanut, E. Clementi, A. Coward, D. Delrosso, C. Ethé, S. Flavoni, T. Graham, J. Harle, D. Iovino, D. Lea, C. Lévy, T. Lovato, N. Martin, S. Masson, S. Mocavero, J. Paul, C. Rousset, D. Storkey, A. Storto, and M. Vancoppenolle. NEMO Ocean Engine, Notes Du Pôle De Modélisation De L'institut Pierre-simon Laplace (IPSL) doi:10.5281/zenodo.1464816, 2017.

McComas, C., and Müller, P.: Time scales of resonant interactions among oceanic internal waves. *J. Phys. Oceanogr.*, 11, 139-147, [https://doi.org/10.1175/1520-0485\(1981\)011<0139:TSORIA>2.0.CO;2](https://doi.org/10.1175/1520-0485(1981)011<0139:TSORIA>2.0.CO;2), 1981.

Olbers, D., and Eden, C.: A global model for the diapycnal diffusivity induced by internal gravity waves. *J. Phys. Oceanogr.*, 43, 1759-1779, <https://doi.org/10.1175/JPO-D-12-0207.1>, 2013.

Pacanowski, R. C., and Philander, S. G. H.: Parameterization of vertical mixing in numerical models of tropical oceans. *J. Phys. Oceanogr.*, 11, 1443-1451, [https://doi.org/10.1175/1520-0485\(1981\)011<1443:POVMIN>2.0.CO;2](https://doi.org/10.1175/1520-0485(1981)011<1443:POVMIN>2.0.CO;2), 1981.

Pickart, R. S., Spall, M. A., Ribergaard, M. H., Moore, G. W. K., Milliff, R. F.: Deep convection in the Irminger Sea forced by Greenland tip jet. *Nature*, 424, 152-156, <https://doi.org/10.1038/nature01729>, 2003.

Pierson, W. J., and Moskowitz, L.: A proposed spectral form for fully developed wind seas based on the similarity theory of S. A. Kitaigorodskii. New York University, School of Engineering and Science, Department of Meteorology and Oceanography: Geophysical Sciences Laboratory Report 63-12, <https://apps.dtic.mil/dtic/tr/fulltext/u2/421610.pdf>, 1963.

Pollmann, F., Eden, C., Olbers, D.: Evaluating the global internal wave model IDEMIX using finestructure methods. *J. Phys. Oceanogr.*, 47(9), 2267-2289, <https://doi.org/10.1175/JPO-D-16-0204.1>, 2017.

Putrasahan, D. A., Lohmann, K., von Storch, J.-S., Jungclaus, J. H., Haak, H., Gutjahr, O.: Surface flux drivers fort he slowdown of the Atlantic Meridional Overturning Circulation in a high-resolution global coupled climate model. *J. Adv. Model. Earth Sys.*, 11, 1349-1363, <https://doi.org/10.1029/2018MS001447>, 2019.

Rippeth, T. P., Lincoln, B. J., Lenn, Y.-D., Green, J. A. M., Sundfjord, A., Bacon, S.: Tide-mediated warming of Arctic halocline by Atlantic heat fluxes over rough topography, *Nature Geoscience*, 8, 191-194, <https://doi.org/10.1038/ngeo2350>, 2015.

Rippeth, T. P., Vlasenko, V., Stashchuk, N., Scanell, B. D., Green, J. A. M., Lincoln, B. J., Bacon, S.: Tidal conversion and mixing poleward of the critical latitude (an Arctic case study), *Geophys. Res. Lett.*, 44, 12349-12357, <https://doi.org/0.1002/2017GL075310>, 2017.

Shu, Q., Wang, Q., Su, J., Li, X., Q. F.: Assessment of the Atlantic water layer in the Arctic Ocean in CMIP5 climate models. *Clim. Dyn.*, 53(9), 5279-5291, <https://doi.org/10.1007/s00382-019-04870-6>, 2019.

Siegelman, L., Energetic submesoscale dynamics in the ocean interior, *J. Phys. Oceanogr.*, doi:10.1175/JPO-D-19-0253.1, 2020.

Taylor, J. R. and R. Ferrari. Buoyancy and wind-driven convection at mixed layer density fronts. *Journal of Physical Oceanography*, 40(6):1222–1242, 2016/06/16, 2010.

Torres, H. S., P. Klein, D. Menemenlis, B. Qiu, Z. Su, J. Wang, S. Chen, and L.-L. Fu, Partitioning ocean motions into balanced motions and internal gravity waves: A modeling study in anticipation of future space missions, *J. Geophys. Res.: Oceans*, 123 (11), 8084–8105, doi:10.1029/2018JC014438, 2018.

Våge, K., Pickart, R. Sarafanov, A., Knutsen, Ø., Mercier, H., Lherminier, P., van Aken, H. M., Meincke, J., Quadfasel, D., Bacon, S.: The Irminger Gyre: circulation, convection, and interannual variability. *Deep-Sea Res. I*, 58, 590-614,

<https://doi.org/10.1016/j.dsr.2011.03.001>, 2011.

Wang, Q., Wekerle, C., Danilov, S., Wang, X., Jung, T.: A 4.5km resolution Arctic Ocean simulation with the global multi-resolution model FESOM 1.4. *Geophys. Model Dev.*, 11, 1229-1255, <https://doi.org/10.5194/gmd-11-1229-2018>, 2018.

Zhang, J. and Steele, M.: Effect of vertical mixing on the Atlantic Water layer circulation in the Arctic Ocean. *Geophys. Res. Oceans*, 112, C04S04, <https://doi.org/10.1029/2006JC003732>, 2007.